

General Disclaimer

One or more of the Following Statements may affect this Document

- This document has been reproduced from the best copy furnished by the organizational source. It is being released in the interest of making available as much information as possible.
- This document may contain data, which exceeds the sheet parameters. It was furnished in this condition by the organizational source and is the best copy available.
- This document may contain tone-on-tone or color graphs, charts and/or pictures, which have been reproduced in black and white.
- This document is paginated as submitted by the original source.
- Portions of this document are not fully legible due to the historical nature of some of the material. However, it is the best reproduction available from the original submission.

NASA CONTRACTOR REPORT 166422

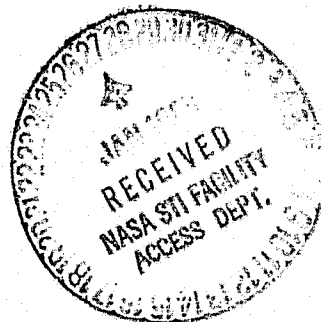
(NASA-CR-166422) EXPERIMENTAL STUDY OF
SURFACE PRESSURES INDUCED ON A FLAT PLATE
AND A BODY OF REVOLUTION BY VARIOUS DUAL JET
CONFIGURATIONS (Virginia Research
Associates, Blacksburg.) 82 p HC A05/MF A01 G3/34

N83-16677

**Unclas
08348**

Experimental Study of Surface Pressure Induced on a Flat
Plate and a Body of Revolution by Various Dual Jet
Configurations

J. A. Schetz
A. K. Jakubowski



CONTRACT NAS2-10437
December 1982

NASA

NASA CONTRACTOR REPORT 166422

**Experimental Study of Surface Pressure Induced on a Flat Plate and a Body
Revolution by Various Dual Jet Configurations**

**Joseph A. Schetz and Antoni K. Jakubowski
Virginia Research Associates
Blacksburg, Virginia**

**Prepared for
Ames Research Center
under Contract NAS 2-10437**



**National Aeronautics and
Space Administration**

**Ames Research Center
Moffett Field, California 94035**

**EXPERIMENTAL STUDY OF SURFACE PRESSURES
INDUCED ON A FLAT PLATE AND A
BODY OF REVOLUTION BY VARIOUS
DUAL JET CONFIGURATIONS**

By

**Joseph A. Schetz and Antoni K. Jakubowski
Virginia Polytechnic Institute and
State University**

SUMMARY

A jet in a crossflow is of interest in practical situations including jet-powered V/STOL aircraft. Three aspects of the problem have received little prior study. First is the effect of the angle of the jet to the crossflow. Second is the performance of dual-jet configurations. The third item for further study is a jet injected from a body of revolution as opposed to a flat plate. The Test Plan for this work was designed to address these three aspects. The experiments were conducted in the 7 x 10 tunnel at NASA Ames at velocities from 14.5 - 35.8 m/sec (47.6 - 117.4 ft/sec.). Detailed pressure distributions are presented for single and dual jets over a range of velocity ratios from 2 to 10, spacings from 2 to 6 diameters and injection angles of 90, 75, 60, and 105 degrees. For the Body of Revolution tests, the ratio of the jet to body diameters was set as large as possible ($\approx 1/2$) to be representative of V/STOL

aircraft applications. The Flat Plate tests involved dual jets both aligned and in side-by-side configurations. The effects of the various parameters and the differences between the axisymmetric and planar body geometrics on the nature, size, shape, and strength of the interaction regions on the body surfaces is shown. Some flowfield measurements are also presented, and it is shown that a simple analysis is capable of predicting the trajectories of the jets.

NOTATION

| | |
|--------------|---|
| C_p | Pressure coefficient |
| ΔC_p | Pressure coefficient difference ($C_{p_{jet\ on}} - C_{p_{jet\ off}}$) |
| D | Diameter, cm |
| \dot{m} | Mass flow rate, kg/sec. |
| M | Mach number |
| P | Pressure, atm |
| q | Dynamic pressure, atm |
| R | Nominal velocity ratio |
| S | Center to center jet spacing, cm |
| T | Temperature, °K |
| V | Velocity, m/sec. |
| x | Streamwise coordinate measured from center of the front nozzle, cm |
| $X = x/D$ | |
| y | Transverse coordinate (arc length for body of revolution) measured from nozzle center plus (+) is to the right looking downstream, cm |
| $Y = y/D$ | |
| ρ | Density, kg/m ³ |
| θ | Injection angle measured from the horizontal, deg. |
| δ^* | Boundary layer displacement thickness, cm |

Subscripts

| | |
|-----------------|---------------------------------|
| b | Main body |
| j | Jet conditions |
| ∞ | Freestream conditions |
| $(\bar{\quad})$ | Averaged quantity over jet exit |

INTRODUCTION

The flowfield produced by a jet in a cross flow is of interest in a number of practical situations ranging from smokestacks and power plant and sewage outfalls to chemical mixing operations to jet-powered V/STOL aircraft. The available information on this flow, in general, is discussed in Ref. (1). For the V/STOL application, the pressure field induced on adjacent surfaces is of particular importance. Thus, there have been a number of detailed experimental studies of that part of the flowfield covering many of the important variables and parameters (see Refs. (2) - (12)). Reviews of the early work can be found in Refs. (13) and (14), and an up to date tabulation of the available information is contained in Ref. (15). The jet generally induces negative (with respect to the freestream) pressures on the nearby surfaces, and this results in a net loss of lift on the body viewed as a whole. The longitudinal variation of the surface pressures is also important, since that determines the resulting pitching moment.

There are three aspects of the general problem that have received little or no careful study. The first is the effect of the angle of the jet with respect to the crossflow. That is important because the transition to wingborne operation is most commonly accompanied by a change in the angle of the jet thrust vector. There are few prior investigations in the literature (see Refs. (8), (11) and (16)). The second item is the performance of dual-jet configurations, either in-line or side-by-side. The mutual interference as a function of center-to-center spacing is the issue here. Again, few references (e.g. Refs. (3), (8) and (17)) exist. The third item identified here as a prime candidate for further study is the behavior of a

jet (or jets) injected from a body of revolution as opposed to the large flat plates usually considered. This is of obvious importance for V/STOL aircraft with lifting jets in the fuselage. One can anticipate substantial transverse pressure "relief" around a cylindrical body. The only previous work found is Ref. (18) which considered a case where $D_{jet}/D_{body} \ll 1$. That is not realistic for V/STOL aircraft where $D_{jet}/D_{body} \approx 1/2$ can be encountered. Lastly, the interplay of the three items mentioned here over a range of the key parameter for all such flows, V_{jet}/V_{stream} , is clearly of importance to the designer.

There have also been a number of analyses and semi-empirical analyses for the jet in a crossflow problem (e.g. Refs. (15), (19) - (28)) that should be mentioned in a discussion of this general flow. None of them, however, can presently treat in a fundamental way the combination of two or more of the three items selected here for study. Hopefully, the experimental studies to be reported here will aid in the generalization of the existing analyses.

The test plan for the present work was designed to provide new information on the influence of the three effects chosen for investigation - 1) injection angle, 2) multiple jets and 3) injection from a body of revolution with $D_{jet}/D_{body} \approx 1/2$. The original Test Matrix planned is shown in Table I. The tests were conducted in the 7 x 10 Subsonic Tunnel at the NASA Ames Research Center. In the succeeding sections of this report, the apparatus, instrumentation, test procedures, test conditions and results will be presented.

APPARATUS

Facility

The experiments were conducted in the 7 ft. (2.13m) x 10 ft. (3.05 m) Subsonic Wind Tunnel at the NASA Ames Research Center at velocities from 14.5 m/sec (47.6 ft/sec) to 35.8 m/sec (117.4 ft/sec) depending upon the jet/freestream velocity ratio desired. This facility is described in Ref. (29).

Test Models

Two basic configurations - a Body of Revolution and a Flat Plate, were used for this work. The Body of Revolution model is shown in Fig. 1. It is 2.06 m (6.75 ft.) long with a diameter of 10.16 cm (4 in.). The model has a wooden, streamlined nose, and it is strut-supported from the rear. The front jet nozzle is always located 0.56 m (1.84 ft) from the nose; the rear nozzle is shifted axially to achieve the various jet spacing considered.

Each nozzle is located in a 10.16 cm (4.0 in) long section that is made from a 10.16 cm (4.0 in) diameter tube split in half longitudinally. There are a number of spacer sections either 5.08 cm (2.0 in) or 10.16 cm (4.0 in) long to occupy the areas ahead of, between and behind the nozzle sections in the arrangements for the various jet spacings. The jets had a 4.92 cm (1.94 in) exit diameter to give $D_{jet}/D_{body} \approx 1/2$. The details of the nozzle design will be described in the next section, but it is important to note here that the large jet diameter caused problems in the model design because of severe internal crowding of air supply lines and pressure tap leads.

On the basis of previous studies of the pressure field near the exhaust, a

detailed coverage of the model surface with pressure taps was clearly necessary. Preliminary layouts indicated that as many as 2000 pressure taps would be required for this two-jet arrangement. That implied not only excessive instrumentation requirements (40 - 50, 48-port Scanivalves) but prohibitive problems with running the pressure leads out through the body. Indeed, it proved impossible to design a model under the given constraints to do so. Thus, it was decided to utilize the presumed right/left symmetry of the flow and locate pressure taps on an asymmetric pattern. Some redundant locations were incorporated to enable checks on the right/left symmetry of the pressure field. Finally, the pressure tap layout was designed with closer spacing in the immediate vicinity of the jets. The final configuration for the 90° injectors is shown in Fig. 2. They are laid out on a grid with values of x/D indicating axial location with respect to the center of the front jet and values of y/D indicating the arc distance off the centerline of the jets. The layout on the spacers was on a simpler pattern as can be seen in Fig. 2(a) which is for the 6 jet diameter spacing arrangement. For the nozzles with injection angles other than 90°, the opening in the body surface becomes elongated. Thus, some of the pressure tap locations near the nozzle for the 90° case are obliterated for the oblique angle cases. With this, 10 48-port Scanivalves were still required.

The nozzle and spacer sections were held in the model by screws along the side centerlines. The joints between the sections were carefully sealed and smoothed with modeling clay and the side seams were taped.

The boundary layer developing along the body was measured at a station in line with the back of the front nozzle at speeds corresponding to 1.0 to 5.0 cm H₂O (12.7 to 28.5 m/s) which covered the lower half of the test range.

The displacement thickness was found to vary from 0.091 cm at the lower speed to 0.067 cm at the higher. These values indicate $\delta^*/D_{jet} \approx 1/50$ which must be considered in the small boundary layer range. The velocity profiles indicated turbulent flow, which is in accord with the values of the Reynolds number based on length. At the lowest speed in the test plan, the Reynolds number based on the length to the center of the front nozzle is 5.6×10^5 .

The Flat Plate Model is shown in Fig. 3. It has a streamlined leading edge, and the bottom is covered with a fairing. There is a large "L" shaped cut out section to accommodate the injector and spacer sections in various combinations to produce the required different center-to-center jet spacings in either the aligned or side-by-side arrangements. The front (or right looking downstream) injector section always remained in the same place. The pressure tap layouts for the injector and spacer sections are shown using the 90° injector as an example. Part of the fixed portion of the plate is also instrumented with pressure taps. The Flat Plate Model had roughly twice as many pressure taps as the Body or Revolution Model.

The surface distance to the center of the front (or right) injector was 54 cm compared to 61 cm for the Body of Revolution Model. Thus, the boundary layer at the front jet in this case may be estimated to be as

$$\delta^*_{Flat Plate} / \delta^*_{Body Rev.} \approx 0.97.$$

Injector Design

The requirement for $D_{jet}/D_{body} \approx 1/2$ caused difficult problems in the design of the jet injectors. It was desired to have a relatively uniform jet exit velocity profile for all injection angles. Non-uniformities in jet exit profiles have been shown to influence the surface pressure field (Ref. (12)),

and we wished to avoid the added complexity introduced thereby. The requirement was to design an air feed system, a plenum chamber, flow straighteners and a nozzle contour to result in a uniform velocity profile, all to fit in a cross-section only twice the diameter of the jet. This had to include cases where the jet was to exit back towards the rear of the model, from whence the feed lines came, at angles up to 45° . Worse yet, there had to be enough room around the rear injector, so that the feed lines to the front injector and the pressure leads to the front injector and the forward spacer sections could pass. The development of a suitable design proved very difficult, and the final configuration was chosen by a process of trial and error that evolved from an initial configuration based on prior experience and intuition. The Flat Plate model did not present serious space problems, so the injector design developed for the Body of Revolution was simply adopted there also. Indeed, some of the same pieces could be used.

The injector design finally chosen can be illustrated for the case of the 90° injector shown in Fig. 4. The air supply is via four, 0.8 cm ID tubes that entered the bottom (from the right in the view shown in Fig. 4). These lines fed passages that exited into the plenum chamber from four, round vents in the bottom. Each vent is topped with a flat disk that is larger than the vent diameter. The air left the vents through four holes around the periphery of each. This configuration was selected in an attempt to distribute the entering flow over the cross-section of the necessarily short (in the flow direction) plenum. Just above the vent exits is a perforated plate with the hole pattern shown which serves as the next step in the flow distribution process. This hole pattern was refined by trial and

error, and different patterns were required for the other injection angles. Above the perforated plate is a smooth contraction down to the jet diameter. This is followed by a flow straightener insert. This insert, shown in Sect. C-C, consists of a 3.0 cm long, thin-wall tube holding a 0.32 cm honeycomb with 20 mesh screening top and bottom. The purpose of the large length/diameter honeycomb is to force the flow to be all in the same direction. The purpose of the screens is to lessen any remaining non-uniformities by accelerated turbulent mixing. The assembly of the injectors and the manner in which the Body of Revolution model goes together is illustrated in Fig. 5. Lastly, three types of jet exit geometry were considered, and they were accomplished by having three different flow straightener sections for each nozzle. The first type had a curved exit to match the contour of the body. The second was flat and flush with the highpoint of the body surface. The last type was flat and perpendicular to the jet injector axis. For the inclined injectors, this results in a protuberance into the main flow out from the body.

After all the work involved, it was gratifying to find that rather uniform exit velocity profiles could be obtained. Some representative measured exit velocity profiles are shown in Fig. 6 a, b, c, and d. These are hand tracings of Pitot pressure profiles recorded about 2. cm above the jet exits in the absence of the main tunnel crossflow. In Fig. 6 a and b, we show an axial and a transverse traverse through the nozzle center of the 90°, front injector. We believe that some of the small scale "structure" evident in these profiles is due to wakes trailing off the honeycomb surfaces. The result of an axial traverse through the center of the 60°, front injector is shown in Fig. 6c. This example, and that for the 45°, front injector in Fig. 6d, do not correspond to the same exit velocity as in Fig. 6 a and b or each

other. The profiles for the inclined injectors are not as uniform as for 90° , but they were judged as quite acceptable. The air supply for the injectors came from the nominally 200 atm. system at Ames. Some difficulties were encountered with adequately controlling the air temperature for a few runs.

Instrumentation

The primary instrumentation for all the tests was a group of 48 - port Scanivalves fitted with either Druck ± 0.07 atm. or Statham ± 0.17 atm. transducers. Each nozzle or spacer section was laboriously hooked up to one or more Scanivalve connectors by small diameter plastic tubing. Each of the bank of 24 Scanivalves was hooked-up to mating sides of Scanivalve connectors. In this way, some or all of the Scanivalves could be fed by pressure signals from the injector and spacer sections needed for a given test configuration without tampering with the plastic tubing hook-ups. The integrity of each lead from every pressure tap was carefully checked one-by-one by applying a known pressure to the tap at the model surface and reading the output from the Scanivalve.

The Scanivalves were operated and the data was obtained from them interactively by the recently developed data acquisition system for the 40 x 80 and 7 x 10 wind tunnels at Ames Research Center. All the data was recorded on tape for subsequent data reduction. In addition, the output from selected instruments could be monitored visually in digital form.

A straight, 3D yaw head probe manufactured by United Sensor was used to obtain mean-flow measurements in the plumes of the jets. The probe had a blunted, conical nose with five pressure ports as shown in Fig. 7.

ORIGINAL PAGE IS
OF POOR QUALITY

The center hole, labeled as #1, was surrounded by the remaining four ports (#'s 2-5) located along the periphery at 90 degrees intervals. The probe stem was sufficiently long so as to extend the tip out of any interference effects induced by the supporting apparatus. Mean velocity, flow angularity and static pressure profiles in the jets were obtained with the 3D yaw head probe. The calibration curves for this probe, details for which are presented in Ref. (30) enable the various mean flow quantities to be determined regardless as to the magnitude of the angularity in any direction. This was the basic advantage of such a calibration procedure as compared to the procedure introduced by Winternitz in Ref. (31) which, although simpler, is valid for a large angle in one direction only.

The dimensionless pressure coefficients for data reduction are:

$$C_{P_{Yaw}} = (P_5 - P_4)/A$$

$$C_{P_{Pitch}} = (P_2 - P_3)/A$$

$$C_{P_{Total}} = (P_1 - P_T)/A$$

$$C_{P_{Static}} = (P_{S_{Avg}} - P_S)/A$$

where $A = P_1 - P_{S_{Avg}}$

$$P_{S_{Avg}} = (P_2 + P_3 + P_4 + P_5)/4$$

Then

$$P_T = P_1 - A C_{P_{Total}}$$

$$P_S = P_{S_{Avg}} - A C_{P_{Static}}$$

The velocity was determined from Bernoulli's equation for incompressible flow, $P_T - P_S = 1/2\rho_\infty V^2 + 1/2\rho_\infty \sqrt{(v')^2}$. The contribution from the term involving the effect of turbulence can be neglected as the expected

error in the velocity corresponding to such an assumption is approximately 1% for turbulence intensity as high as 14%. The total velocity vector was, therefore, determined as

$$|V| = \sqrt{\frac{2(P_T - P_S)}{\rho_\infty}}$$

This quantity was combined with pitch and yaw angles determined from $C_{p_{Yaw}}$ and $C_{p_{Pitch}}$ to produce velocity vector plots. For these tests, the probe was oriented pointed down 45° towards the model.

All the other necessary measurements were also run through the data acquisition system. These included pressure measurements for tunnel speed and orifice readings for injector mass flow and temperature readings for the tunnel and injector air flows. The barometer and room temperature were read by eye, and the information was entered into the data acquisition system manually.

TEST PLAN AND PROCEDURES

One could obtain the desired range of jet to freestream velocity ratios by a variety of paths including holding the freestream velocity constant and varying the jet velocity or vice versa. There is some appeal to testing at a constant freestream velocity, because that would keep the body Reynolds number and the boundary layer thickness constant. However, the difficulties and effort required to achieve reasonably uniform jet exit velocity profiles not just at one or a few conditions but over a range in jet average velocity of 5:1 ($2 \leq R \leq 10$) was judged to be so severe as to justify the choice of holding the jet velocity fixed and varying the freestream. As a check on the influence of the body Reynolds number variation thus introduced, one case at the same "R", but with a different freestream velocity was included for most configurations tested.

There were three other constraints that influenced the test plan. First, it was thought important to keep the minimum body Reynolds number based on the surface distance to the first nozzle above a certain value, picked as 5×10^5 , to have a turbulent boundary layer. This meant a freestream velocity above roughly 13 m/sec. Second, to avoid the added complexity of strong compressibility effects, it was decided to keep the maximum jet velocities below roughly 120 m/sec ($M_j < 0.35$). Lastly, the pressure drop through the most severely inclined injectors was large enough to limit the mass flow (and thus the jet velocity) that could be obtained for those configurations.

Taking all of the items above into account, a test plan was adopted that had a nominal jet volume flow rate of $0.214 \text{ m}^3/\text{sec}$ corresponding to $\bar{V}_j = 112.5 \text{ m/sec}$ and freestream velocities corresponding to $1.28 \leq q \leq 8.03 \text{ cm. H}_2\text{O}$ ($14.5 \leq V_\infty \leq 36.2, \text{ m/s.}$).

The air supply pressure settings to give the desired flow rates through the various nozzles were found by examining the results of exit velocity traverses such as shown in Fig. 6a, b, c and d for each nozzle in every set. This was necessary, since the feed lines to the front and rear nozzles were of different lengths resulting in different pressure drops.

Each test series was run as follows. First, the data acquisition system was run to obtain "null" readings and calibration settings. The air supply pressure settings corresponding to the set of injectors in use were then brought up and adjusted. Next, the tunnel was turned on to the lowest speed in the series. The data acquisition system was run. The tunnel speed was adjusted to the next setting, and the process was repeated over the range desired. The last point in each series was a single value of "R" achieved at a different combination of tunnel and jet speed than the point at the same "R" in the main series. The tunnel and air supply were turned off, and "null" readings were again taken.

The injectors and/or spacers were then rearranged to obtain the next configuration desired. A test series as described was then run, and so on.

RESULTS

General

The data was reduced and the results are presented here as

$$\Delta C_p = (C_{p_{\text{jet on}}} - C_{p_{\text{jet off}}})$$

as a function of spatial location on the body surface for each configuration. In this way, the first-order effects of any asymmetries or surface irregularities on the models should be normalized out. Before being accepted, each set of data was examined against some qualification criteria. The first group of these involved the jet injection conditions. Was the mass flow (and thus \bar{V}_j) set close enough to the desired nominal conditions? For the two-jet tests, were the mass flows set close enough to each other? For these items, a tolerance of roughly $\pm 5\%$ was adopted. Next, when combined with the actual tunnel speed for a given data point, was the desired value of "R" achieved within again roughly $\pm 5\%$? These questions were important, since we wished to make case-to-case comparisons such as the effect of jet spacing holding "R" nominally fixed, etc. The next examination of the acceptability of the data centered on the right/left symmetry of the flow. For that purpose, the ΔC_p 's from the redundant ports at $x/D = 0$ and $x/D = S/D$ (i.e. the axial stations corresponding to the center of the nozzle exits) and $Y = 0.625$ and 0.875 to the right and left were compared. Here, it was found necessary to adopt the cruder tolerance of $\pm 15\%$. Data for a number of runs had to be discarded on this basis. There was no particular pattern to the occurrence of these "bad" runs. Such a run was sometimes found in the middle of a continuous test series of acceptable runs.

Due to time limitations and some problems with the newly operational data acquisition system, it was not possible to complete the entire test matrix as originally planned. The test matrix that was run still encompassed a very large number of conditions and configurations, so only selected results are presented in this report.

Body of Revolution

Surface Pressure Distributions

The data is presented as plots of axial and transverse variations of ΔC_p . The axial plots are for $y/D = 0.0, 0.248, 0.480, 0.682$ and 0.842 for the Body of Revolution.

The results obtained for $R = 7.7, 90^\circ$ injection through nozzles with exits contoured to the body surface at a spacing of 2.0 diams. are shown in Fig. 8 as open circles. The results obtained for injection from the front nozzle only with the exit of the rear nozzle carefully covered by tape are shown as the solid circles. That notational practice is followed throughout. Looking at the single jet results first, the expected pattern of negative C_p 's is evident. The magnitude of the pressure coefficients near the injectors agrees with those found on flat plates. The influence of the round main body compared to a flat plate case is evidenced as a faster decay in the maximum C_p with y/D , that is, perpendicular to the flow direction. The comparison is somewhat equivocal at this point in our presentation, since the current work used a much denser pattern of pressure taps near the injector than some of the earlier studies. Also, it must be remembered that we are giving ΔC_p so the main effects of the body itself are removed. The dual jet results show that the influence of the rear jet is less than that of the front jet at this close spacing. On the other hand, the presence of the rear jet seems to strengthen the influence of the front jet slightly. An appreciation of the right/left symmetry found can be gained from the transverse variations plotted in Fig. 9 for this

same case.

The effects of the important parameter $R = V_j/V_\infty$ is illustrated by the data in Fig. 10 for $R = 3.2$ at 90° with a contoured exit. The patterns are quite similar to those for $R = 7.7$ in Fig. 8, however, one must recall that C_p denotes the pressure difference Δp normalized with the freestream dynamic pressure, which is different for the two cases. The differences in C_p are largest with increasing lateral distance and in the vicinity of the second jet.

The possible influence of different Reynolds numbers based on length along the body to the first jet at the same dimensionless velocity ratio, R , was studied by running some tests at the same R but different V_∞ . Some results are shown in Fig. 11 for a case with $R \approx 3$, 90° the contoured injector with injection from the front nozzle only. The case shown had a Reynolds number effect larger than was found in most cases, and the effect is generally rather small.

Another variable considered in these tests was the geometry of the nozzle exit. The results presented so far corresponded to the presumably simplest case of the nozzle exits contoured to the curved body surface. In Figs. 12 and 13 results for a flat topped nozzle at $R \approx 8$ and ≈ 3 , 90° and $S/D = 2$ are given, and these may be compared to the contoured nozzle results in Figs. 8 and 10. As might be expected, there are large effects between the nozzles. Also, the magnitude of the largest (absolute values) C_p 's is reduced and the lateral decay seems faster. Lastly, the influence of exit geometry is found to be larger at the higher velocity ratio.

The results of increasing S/D to 4.0 and the 6.0 at 90° with a contoured nozzle exit are shown in Figs. 14 and 15 for $R = 4.7$. The

results in Fig. 14 show that the rear jet is still strongly "sheltered" by the front jet at $S/D = 4.0$. Now, however, the presence of the rear jet slightly reduces the influence of the front jet as opposed to the results in Figs. 8 and 10 for $S/D = 2.0$. The data presented in Fig. 15 is for both jets operating at $R = 4.7$, 90° with contoured injectors at $S/D = 2.0$, 4.0 and 6.0 . Note, that the data for the lesser spacings has been "shifted" downstream to overlay the $S/D = 6.0$ data for the rear nozzle. Here, one can see that the influence of the rear on the front jet is reduced as S/D is increased from 2.0 to 4.0 to 6.0 . The pattern in front of the rear jet changes sharply with S/D from 2.0 to 4.0 , but only slightly from 4.0 to 6.0 .

The influence of injection angle for flat topped nozzles is displayed in Figs. 16 - 19. The results in Fig. 16 for $R \approx 8$ and $S/D = 2.0$ at 75° can be compared with those in Fig. 12 for 90° . The peak values near the front jet are increased slightly and those near the rear jet are increased more, especially at greater lateral distances. The C_p values between the jets tend to be slightly more negative. The general trends continue for the 60° case in Fig. 17, but a new feature also appears. A "peak and valley" pattern appears next to jets. This is very pronounced at $y/D = .682$ near the front jet. This pattern was not observed at 90° or 75° (see Figs. 12 and 16). The same pattern is seen in Fig. 18 for $R \approx 4$ at 60° . At this lower velocity ratio, the rear jet decreases the influence of the front jet on the body surface. For all the inclined jet cases, the influence of each jet is about the same indicating that there is little "sheltering" even at this close $S/D = 2.0$. This behavior is clearest at the higher R 's.

The effect of increased spacing to $S/D = 4.0$ for the inclined jets is shown in Fig. 19 for $R \approx 8$ at 60° . The "peak and valley" pattern is repeated, and the influence of the rear jet on the front and vice versa is slight. All our results indicate only a small effect of spacing for $S/D > 4.0$.

Flowfield Measurements

To amplify on the surface pressure data, some limited measurements of the jet flowfield above the surface were made with the yawhead probe described earlier. A plot of the local velocity vectors in the plane of the jets for $R = 6.5$ at 90° is shown in Fig. 20 for injection from the front nozzle alone. The trajectory of the jet can be seen, and the high penetration across the main flow is clear. The same type of presentation for $R = 3.2$ in Fig. 21 shows the sharply reduced penetration that results. The intersection region with two jets with $R = 6.5$ is displayed in Fig. 22. One can observe that the rear jet is "sheltered" strongly by the front jet; the trajectory of the rear jet is nearly vertical until the intersection.

The ability of the simple analysis of Ref. (28) to predict the trajectory of single and dual jets at various velocity ratios is demonstrated for two cases in Figs. 23 and 24. Obviously, the main features of the flow are accurately predicted. It should be possible to extend this trajectory analysis to predict surface pressures.

Flat Plate Model

Pressure Distributions

Longitudinal pressure distributions at selected lateral distances are plotted in Fig. 25 for the 90° injectors at $R = 6$ with a spacing of two diameters and the jets aligned one behind the other. The results for both jets are shown as open circles, and those for the front jet only are solid circles. This is the same type of plot as used for the Body of Revolution results. The data in Fig. 25 can, thus, be roughly compared to Fig. 8 for the Body of Revolution at $R = 7.7$. First, one can note that there are no positive C_p values behind the second jet on the Flat Plate. Second, the peak values on the Body of Revolution are somewhat higher very near the nozzles. Third, by comparing values at $y/D \approx 0.8$, it can be seen that the peak values definitely decay faster with lateral distance on the Body of Revolution. In general, however, the qualitative observations made earlier about the Body of Revolution cases also hold here.

The effects of the important parameter R can be seen in the isobar plots in Figs. 26, 27, and 28 for $R = 4, 6$ and 8 . As R increases, the area of the surface influenced by the jets increases. This increase is mostly in terms of the areas with small to moderate negative values of C_p (e.g. $0 \leq C_p \leq -1.0$). The area with $C_p \leq -1.0$ does not change significantly with R . Since the area of influence increases with R , the total normal force also increases with R , but the increase is slow. Thus, the value of the total normal force normalized with the thrust of the jets actually decreases with increasing R . The effective center of normal force moves forward with increasing R . Estimates indicate that this center coincides

with the center of the front jet at about $R = 10$. Lastly, the shape of the interaction region changes with increasing R . At low R , the isobars show asymmetrical lobes displaced in the downstream direction. At higher R , there is less downstream distortion. Compare Fig. 26 at $R = 4$ to Fig. 28 at $R = 8$.

The present results in Fig. 28 can be roughly compared with those of Wooler et al in Ref. (32) at $R = 8$ but, $S/D = 2.5$ as opposed to our $S/D = 2.0$. The comparison is made difficult, since the tests in Ref. (32) did not have as detailed a coverage of the area near the jets as here. Nonetheless, comparison of the $C_p = -0.5$ isobars for example, shows rather good agreement in terms of overall shape and axial and lateral extent.

The effects of increasing the dimensionless spacing, S/D , from 2 to 4 with 90° and $R = 6$ are shown in Figs. 29 and 30. The plots in Fig. 29 can be compared to those in Fig. 14, although that data is for a lower $R = 4.7$. Here, as for the Body of Revolution, the rear jet is still sheltered by the front jet and the influence of the front jet on the flow is reduced by the presence of the rear jet. Looking at the isobar patterns in Fig. 30 and comparing with those in Fig. 27 for the same case with $S/D = 2$, one can observe that the only overlap of the interaction regions of the two jets is now for small C_p values only. Comparing isobar plots with the front jet only (not presented here due to space limitations) with those for both jets operating shows that the interaction of the two jets increases the surface area influenced by the front jet. The merging of the interaction regions was also found to be influenced by the velocity ratio, R . The merging is most pronounced at low R values. Also, the sheltering of the rear jet reduces the downstream distortion of its flow interaction area.

The influence of injection angle at $R = 6$ is shown in the next series of figures. Figs. 31 and 32 have results for a 75° angle, and Figs. 33 and 34 have results for upstream injection at 105° , all at $S/D = 4$. The 75° results can be crudely compared to those in Fig. 16, but this is confused by the fact that those data are for the flat top nozzle exit and $S/D = 2$. The isobar plots in Figs. 32 and 34 and that for 90° in Fig. 30 show some interesting effects. The change from 75° to 90° produces only slight changes in the total interaction area influenced by the jets and, thus, in the normal force. However, the change from 90° to 105° leads to an increase in the total interaction area and, hence also the normal force. Further, as the angle goes from 75° to 90° to 105° , the effective center of the interaction region moves forward. The plots in Figs. 29 and 33 indicate that the region ahead of the front jet is influenced somewhat more strongly by upstream angled injection. In addition, the sheltering of the rear jet by the front jet is stronger for 105° than for 90° or 75° injection.

The result of reduced spacing to $S/D = 2$ at 75° and $R = 6$ can be noted by comparing Figs. 35 and 36 with Figs. 31 and 33 for $S/D = 4$. The effects are generally the same as for 90° injection.

The data taken for 60° injection on the Flat Plate model all showed very unsymmetrical (right/left) surface pressure patterns. For that reason, none of those results are included here. It is hoped that those tests can be repeated.

The next series of figures present the results obtained with two jets in a side-by-side arrangement. Due to test time limitations fewer parameters were varied in this configuration. All the data obtained are for the 90° injectors only.

Transverse pressure distributions at five axial stations, including one ahead of the jets, are shown in Fig. 37 for $R = 6$ and $S/D = 2$. Data for only the right jet operating are shown as solid circles. The presence of the left jet has a slight effect on the right jet at the station ahead of the jets ($x/D = -.825$), but the interference effect is quite large at $x/D = 0$ and the downstream stations. High (negative) ΔC_p values are obtained between and just downstream of the jets. Also, the right/left symmetry of the flow can be seen to be good for single and dual jet runs. This is illustrated more specifically in Fig. 38 where axial pressure distributions at presumably symmetric transverse locations are shown. Perfect symmetry would have the crosses and circles on top of each other. Here, as in all the cases tested, the best symmetry was found in the range $4 \leq R \leq 8$. At the highest and lowest velocity ratios, the symmetry achieved was the poorest. An isobar map for the same case as in Figs. 37 and 38 is given in Fig. 39.

Figs. 40 and 41 and 42 and 43 show pressure distributions and isobar maps for $S/D = 2$ with $R = 4$ and 8 . Comparing these with Figs. 37 and 39, the effects of R can be seen. As R is increased, there is a pronounced increase in the size of the interaction region around the jets. The interaction normal force also increases, both as a result of the increase in area effected and increases (negative) in the ΔC_p values near the orifices. This latter point can be seen by comparing the distributions at $x/D = 0.0$

in Figs. 37, 40, and 42 for $R = 4, 6$ and 8 , respectively. The effective center of the interaction force shifts upstream as R is increased. Taken altogether, these results indicate a strong increase in the interaction between the two jets as R is increased at this close spacing, $S/D = 2$. The large (negative) ΔC_p values in the region immediately behind the jets along the line of symmetry between them at the high R 's is noteworthy. This is probably a result of the interaction between the pairs of counter-rotating vortices formed in each jet.

The influence of increasing S/D to 4 at $R = 6$ can be seen by comparing the results in Figs. 44 and 45 to those given earlier for $S/D = 2$ at the same R in Figs. 37 and 39. The interaction of the jets is diminished significantly. This can be seen both by comparing the results with and without the left jet operating in Fig. 44 and by comparing the distributions at $x/D = 0.495$, for example, in Figs. 37 and 44. Looking at the isobar maps, one can see that there is much less overlap of the interaction regions of the two jets at $S/D = 4$. The overlap or merging of the interaction regions is R dependent; it is strongest at the higher R values. The interaction region of each jet on the "free" side (the side away from the other jet) is still always larger than for the single jet even at $S/D = 4$.

CONCLUSIONS

An examination of the available prior literature for the interaction of a jet in a crossflow with an adjacent surface reveals that there were three prominent areas that required further study. The first was the influence of the angle of jet injection with respect to the main stream. The second was the performance of dual-jet configurations at various spacings, including aligned and side-by-side arrangements. The third was the differences between injection from a flat plate and a body of revolution especially where the jet diameter is an appreciable fraction ($\approx 1/2$) of the body diameter. The mutual interaction of these three topics is also, obviously of importance. A Test Plan to meet these objectives was designed and carried out in the 7 x 10 tunnel at NASA Ames Research Center.

The numerous findings of these studies are presented in detail along with the data in the Results section. In brief summary here, it can be stated that the three topics selected for study were all found to have strong effects on the nature, size, shape and strength of the interaction region produced on the body surface by the jet(s).

Table I PLANNED TEST MATRIX

Configurations

1. Body of revolution with tandem jets
2. Flat Plate with tandem dual jets
3. Flat plate with transverse dual jets

Parameter Variations

| Jet Injection Angle, degrees | Jet Spacing, multiples of jet diameter | Jet to Freestream Velocity Ratio | | | | |
|---------------------------------|--|----------------------------------|---|---|---|----|
| | | 2 | 4 | 6 | 8 | 10 |
| 45 | 2 | 2 | 4 | 6 | 8 | 10 |
| | 3 | " | " | " | " | " |
| | 4 | " | " | " | " | " |
| | 5 | " | " | " | " | " |
| | 6 | " | " | " | " | " |
| 60 | 2 | " | " | " | " | " |
| | 3 | " | " | " | " | " |
| | 4 | " | " | " | " | " |
| | 5 | " | " | " | " | " |
| | 6 | " | " | " | " | " |
| 75 | 2 | " | " | " | " | " |
| | 3 | " | " | " | " | " |
| | 4 | " | " | " | " | " |
| | 5 | " | " | " | " | " |
| | 6 | " | " | " | " | " |
| 105 | 2 | " | " | " | " | " |
| | 3 | " | " | " | " | " |
| | 4 | " | " | " | " | " |
| | 5 | " | " | " | " | " |
| | 6 | " | " | " | " | " |
| 90 | 2 | " | " | " | " | " |
| | 3 | " | " | " | " | " |
| | 4 | " | " | " | " | " |
| | 5 | " | " | " | " | " |
| | 6 | " | " | " | " | " |

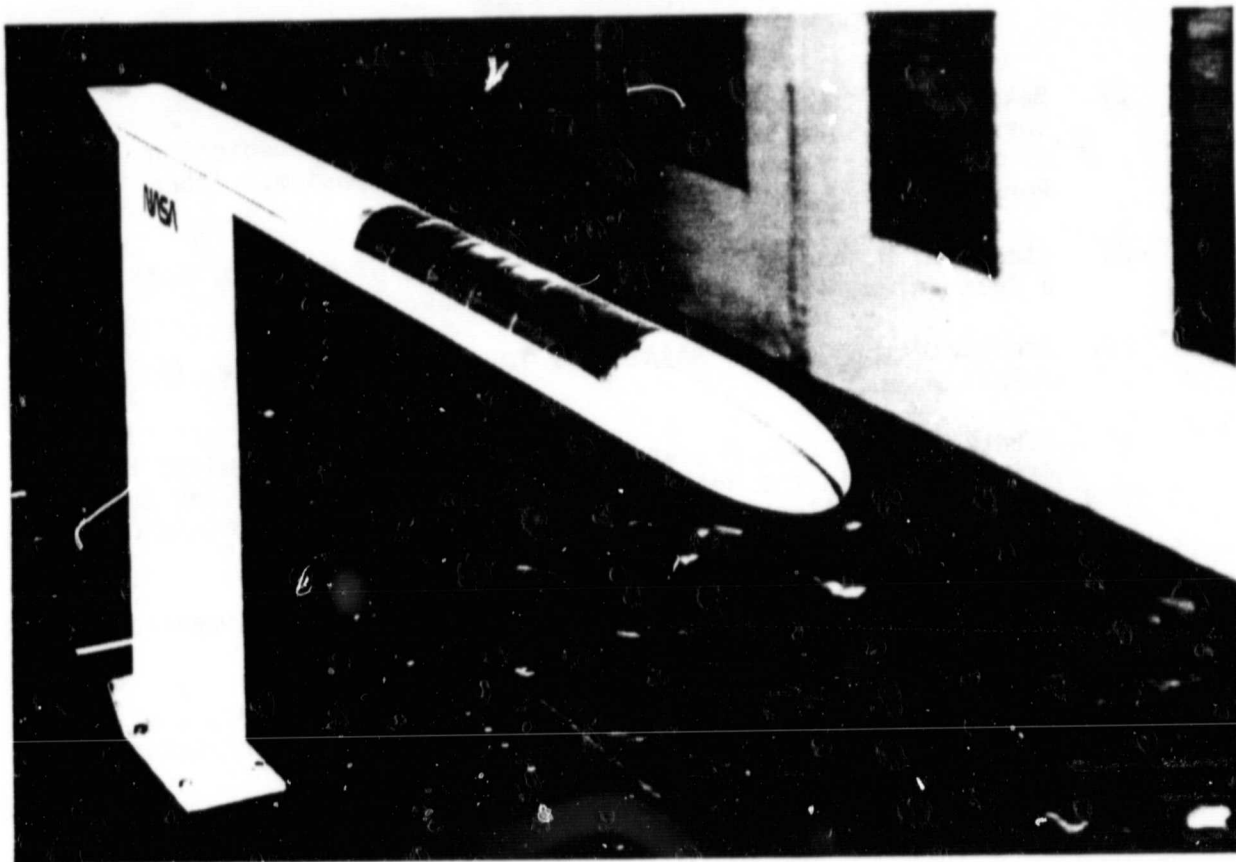
REFERENCES

1. Schetz, J. A.: Injection and Mixing in Turbulent Flow, AIAA, New York, 1980.
2. Vogler, Raymond D.: Surface Pressure Distributions Induced on a Flat Plate by a Cold Air Jet Issuing Perpendicularly From the Plate and Normal to a Low-Speed Free-Stream Flow. NASA TN D-1629, 1963.
3. Vogler, Raymond D.: Interference Effects of Single and Multiple Round or Slotted Jets on a VTOL Model in Transition. NASA TN D-2380, August 1964.
4. Bradbury, L. J. S.; and Wood, M. N.: The Static Pressure Distributions Around a Circular Jet Exhausting Normally From a Plane Wall Into an Airstream. C. P. No. 822, Brit. A. R. C., 1965.
5. Margason, Richard J.: Jet-Induced Effects in Transition Flight. Conference on V/STOL and STOL Aircraft, NASA SP-116, 1966, pp. 177-189.
6. Gentry, Garl L.; and Margason, Richard J.: Jet Induced Lift Losses on VTOL Configurations Hovering In and Out of Ground Effect. NASA TN D-3166, February 1966.
7. Soullier, A.: Testing at SI. MAS for Basic Investigation on Jet Interactions. Distributions of Pressures Around the Jet Orifice. NASA TTF-14066, April 1968.
8. Fricke, L. B.; Wooler, P. T.; and Ziegler, H.: A Wind Tunnel Investigation of Jets Exhausting Into a Crossflow. AFFDL-TR-70-154, Vols. I-IV, U. S. Air Force, Dec. 1970.
 Vol. I - Test Description and Data Analysis
 Vol. II - Additional Data for the One-Jet Configuration
 Vol. III - Additional Data for Two-Jet Configurations
 Vol. IV - Additional Data for the Three-Jet Configuration
9. Margason, Richard J.: Review of Propulsion-Induced Effects on Aerodynamics of Jet/STOL Aircraft. NASA TN D-5617, February 1970.
10. Fearn, R. L. and Weston, R. P., "Induced Pressure Distribution of a Jet in a Crossflow," NASA TN D-7916, June 1975.
11. Taylor, P., "An Investigation of an Inclined Jet in a Crosswind," Aeronautical Quarterly, Vol. XXVIII, Part I, February 1977.
12. Kuhlman, J. M., Ousterhout, D. S., and Marcup, R. W.: Experimental Investigation of Effects of Jet Decay Rate on Jet-Induced Pressures on a Flat Plate: Tabulated Data. NASA CR-158990, Nov. 1978.
13. Lee, C. C.: A Review of Research on the Interaction of a Jet With an External Stream, Tech. Note R-184, (Contract No. DA-01-021-AMC-11528(z)), Res. Lab., Brown Engineering Co., Inc., Mar. 1966. (Available from DDC as AD 630 294).

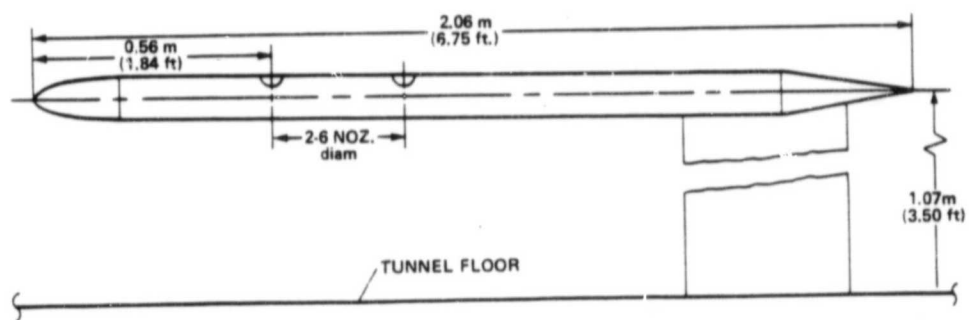
14. Garner, Jack E.: A Review of Jet Efflux Studies Application to V/STOL Aircraft. AEDC-TR-67-163, U. S. Air Force, Sept. 1967. (Available from DDC as AD 658 432).
15. Perkins, S. C. Jr. and Mendenhall, M. R.: "A Study of Real Jet Effects on the Surface Pressure Distribution Induced by a Jet in a Crossflow," NASA CR-166150, Mar. 1981.
16. Margason, Richard J.: The Path of a Jet Directed at Large Angles to a Subsonic Free Stream. NASA TN D-4919, November 1968.
17. Ziegler, H. and Wooler, P. T.: Analysis of Stratified and Closely Spaced Jets Exhausting into a Crossflow. NASA CR-132297, Nov. 1973.
18. Ousterhout, D. S.: An Experimental Investigation of a Cold Jet Emitting from a Body of Revolution into a Subsonic Free Stream. NASA CR-2089, July 1972.
19. Abramovich, G. N.: The Theory of Turbulent Jets. M.I.T. Press Co., 1963, pp. 541-552.
20. Wu, J. C.; and Wright, M. A.: A Blockage-Sink Representation of Jet Interference Effects for Noncircular Jet Orifices. Analysis of a Jet in a Subsonic Crosswind, NASA SP-218, 1969, pp. 85-99.
21. Street, Troy, A.; and Spring, Donald J.: Experimental Reaction Jet Effects at Subsonic Speeds. Analysis of a Jet in a Subsonic Crosswind, NASA SP-218, 1969, pp. 63-83.
22. Dietz, W. E., Jr.: A Method for Calculating the Induced Pressure Distribution Associated with a Jet in a Crossflow. M. S. Thesis, Florida University, 1975 (also available as NASA CR 146434, 1975).
23. Yen, K. T., "The Aerodynamics of a Jet in a Crossflow," NADC-78291-60, December 1978.
24. Perkins, S. C., Jr. and Mendenhall, M. R., "A Correlation Method to Predict the Surface Pressure Distribution on an Infinite Plate or a Body of Revolution from which a Jet is Issuing," NASA CR 152345, January 1980.
25. Fearn, R. L., Kalota, C., and Dietz, W. E., Jr., "A Jet Aerodynamic Surface Interference Model," Proceedings V/STOL Aircraft Aerodynamics, Vol. 1, Naval Post Graduate School, Monterey, California, May 1979.
26. Campbell, J. F. and Schetz, J. A.: Analysis of the Injection of a Heated Turbulent Jet into a Cross Flow, NASA TR R-413, Dec. 1973.

27. Baker, A. J., Manhardt, P. D. and Orzechowski, J. A.: A Three-Dimensional Finite Element Algorithm for Prediction of V/STOL Jet-Induced Flowfields, AGARD Symposium, Lisbon, Portugal, Nov. 1981.
28. Isaac, K. M. and Schetz, J. A.: Analysis of Multiple Jets in a Cross-flow, ASME Paper 82-WA/FE-4, Nov. 1982.
29. Ames Research Center, NASA: 7 x 10 Wind Tunnel Guide, Oct. 1978.
30. Schetz, J. A., Lee, H., and Kong, F., "Mean and Turbulent Flow Measurements in the Near-Wake Region of a Self-Propelled Submarine-and/or Airship-Like Model at Pitch or Yaw," VPI-Aero-097, Sept. 1979.
31. Winternitz, F. A. L., "Probe Measurements in Three-Dimensional Flow," Aircraft Engineering, August 1956.
32. Wooler, P. T., Wasson, H. R., Kao, H. C., Ziegler, H., and Schwandemann, M. F., "V/STOL Aircraft Aerodynamic Prediction Methods Investigation," AFFDL-TR-72-26, Jan. 1972.

ORIGINAL PAGE
BLACK AND WHITE PHOTOGRAPH



(a) - Photograph of the Model
in the Wind Tunnel.



(b) - Dimensioned Sketch

Fig. 1 - Body of Revolution Model

ORIGINAL PAGE 19
OF POOR QUALITY

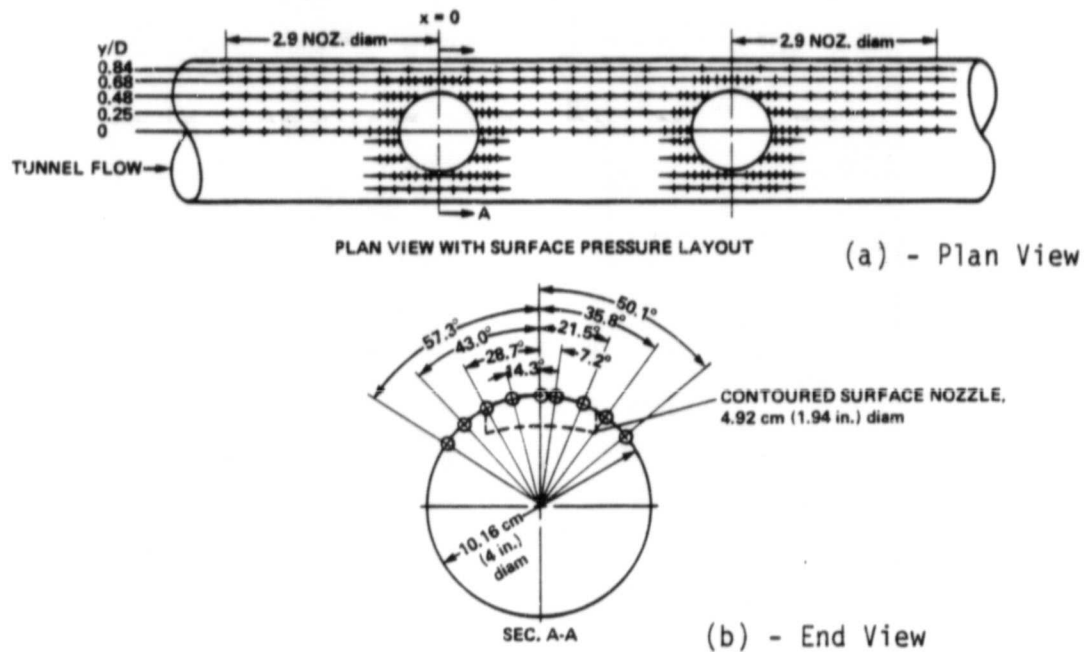


Fig. 2 - Pressure Tap Layout for Body
of Revolution Model

ORIGINAL PAGE IS
OF POOR QUALITY



(a) - Photograph of the Model in
the Wind Tunnel.

Fig. 3 - Flat Plate Model

ORIGINAL PAGE IS
OF POOR QUALITY



Fig. 3(b) - Close-up of the Nozzle
Section.

ORIGINAL PAGE 13
OF POOR QUALITY

ALL DIM. IN CM.

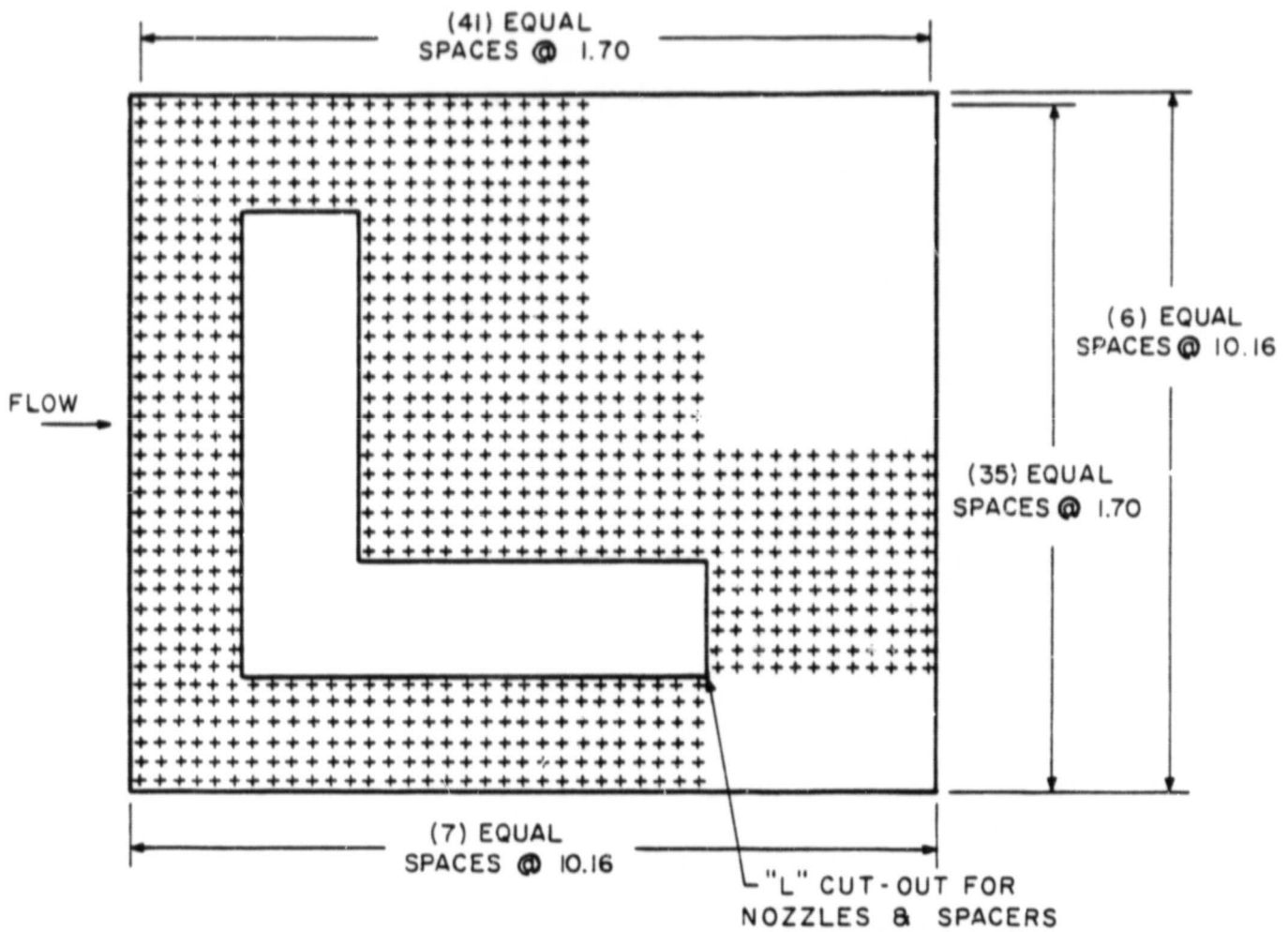


Fig. 3(c) - Pressure Tap Layout in the Instrumented Section of the Model.

ORIGINAL PAGE IS
OF POOR QUALITY

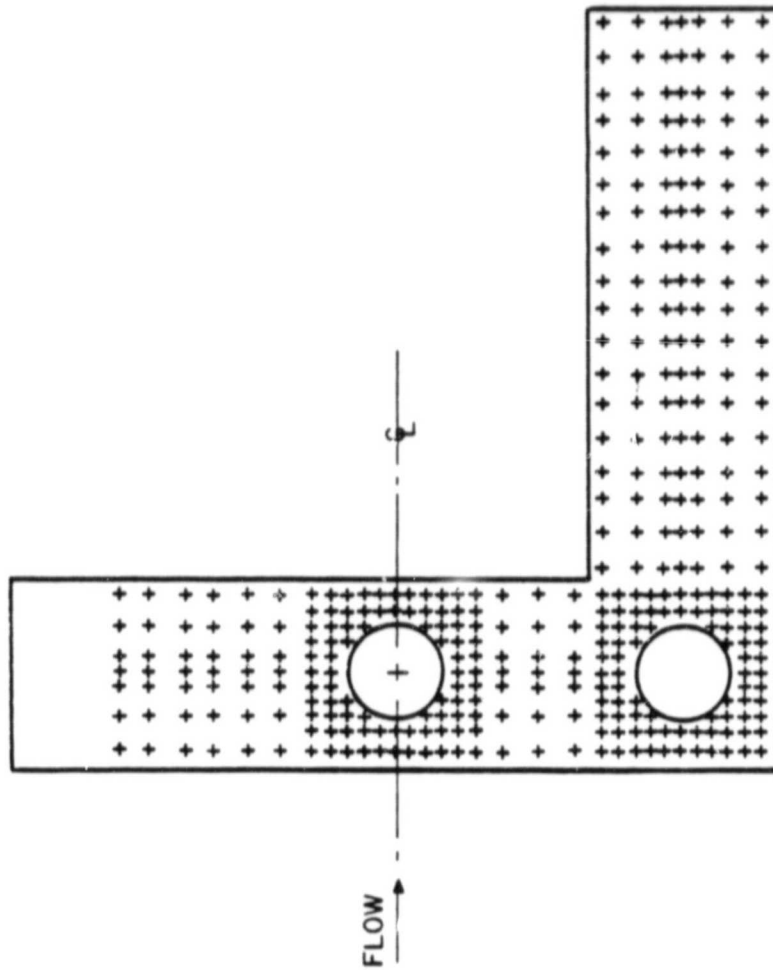


Fig. 3(d) - Pressure Tap Layout in the
Nozzle and Spacer Section.

ORIGINAL PAGE IS
OF POOR QUALITY

ORIGINAL PAGE IS
OF POOR QUALITY

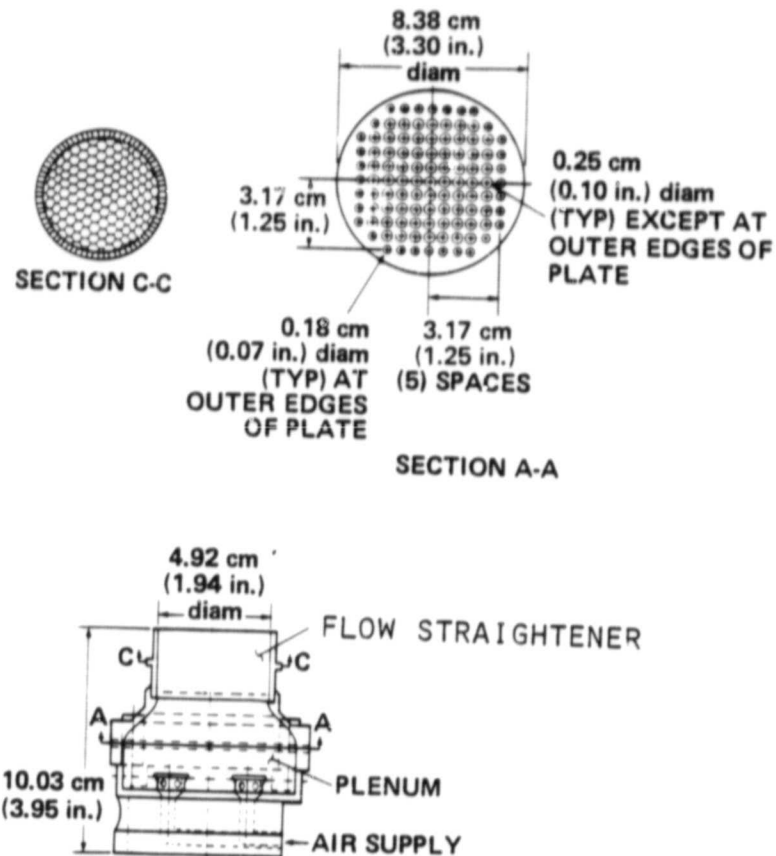


Fig. 4 - Details of the Injector
Design for the 90° Case.

ORIGINAL PAGE IS
OF POOR QUALITY

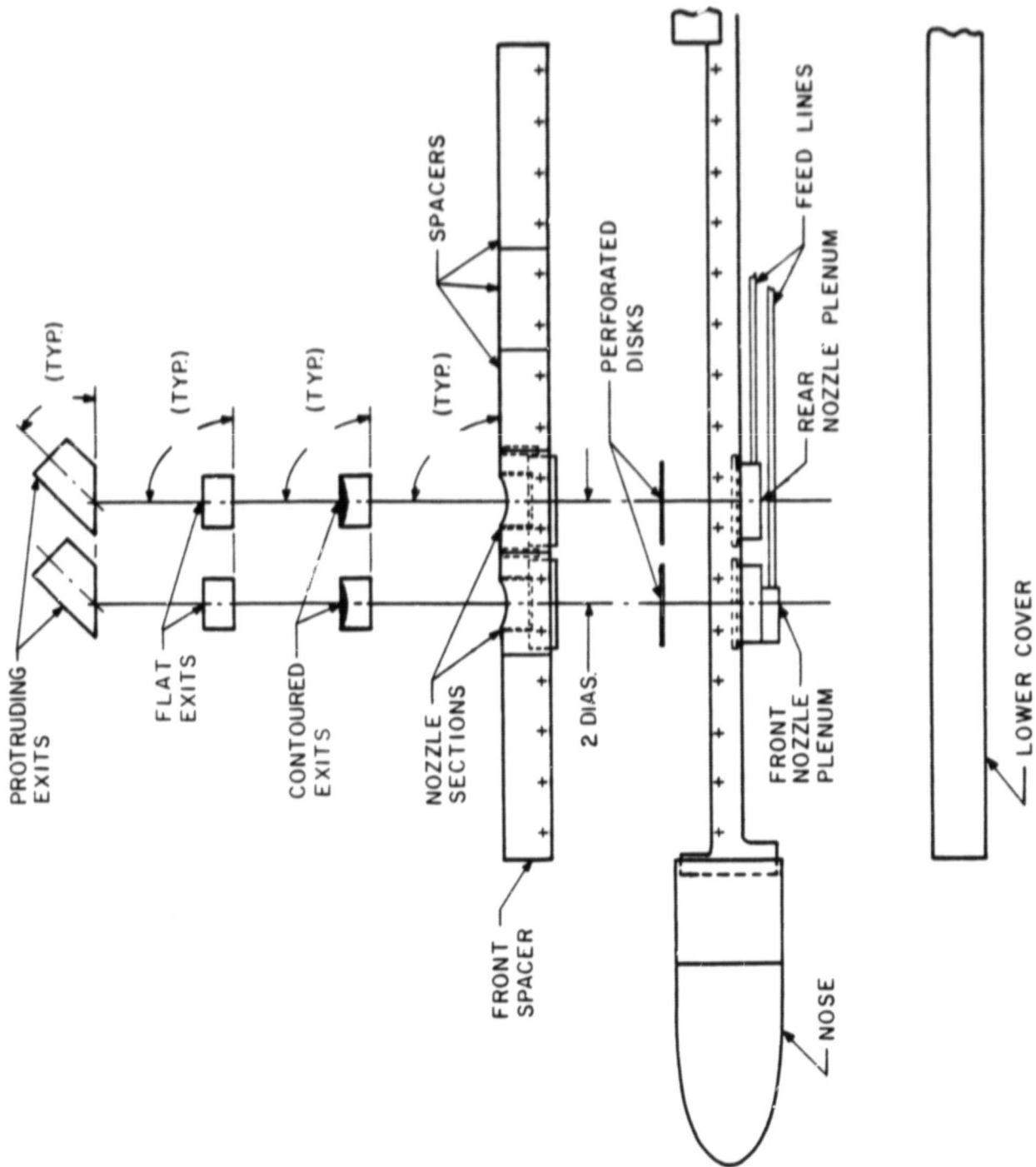
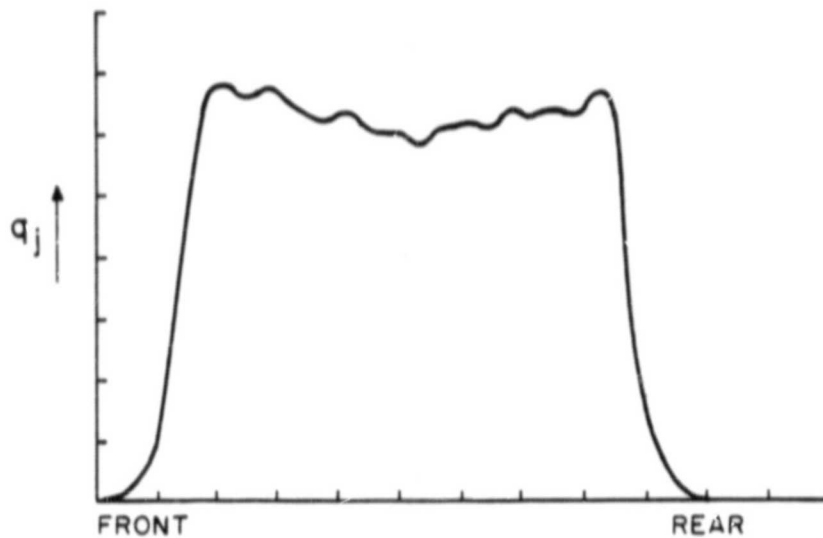
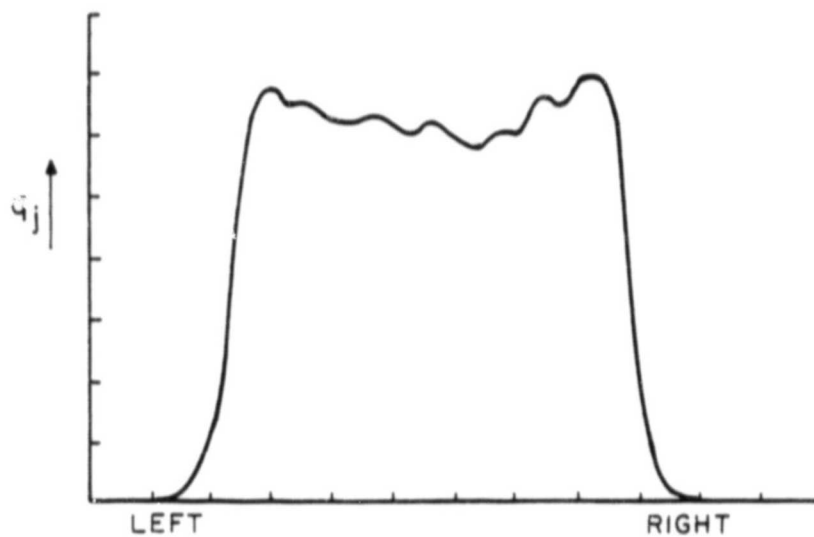


Fig. 5 - Exploded View of the Body of Revolution Model Showing the Assembly.

ORIGINAL PAGE IS
OF POOR QUALITY
OF POOR QUALITY
OF POOR QUALITY



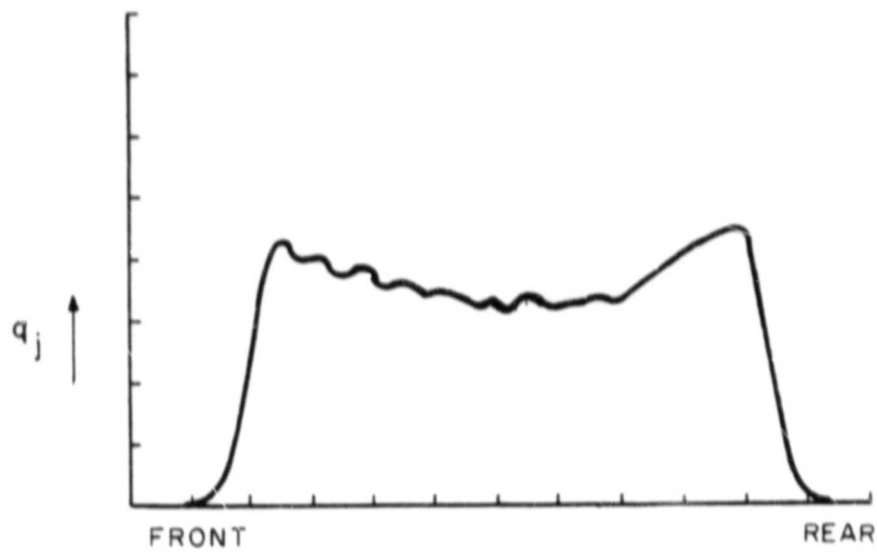
(a) 90°, "X" TRAVERSE



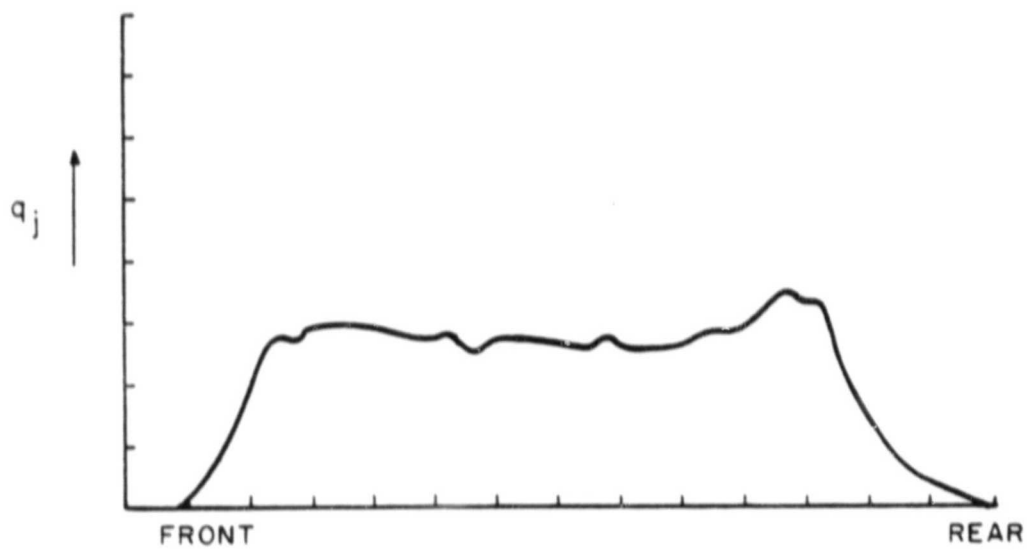
(b) 90°, "Y" TRAVERSE

Fig. 6 - Typical Pitot Tube Surveys
Across the Exit of the
Nozzles in the Absence of
Crossflow.

ORIGINAL PAGE 13
OF POOR QUALITY



(c) 60°, "X" TRAVERSE



(d) 45°, "X" TRAVERSE

Fig. 6 - (Cont'd.)

ORIGINAL PAGE IS
OF POOR QUALITY

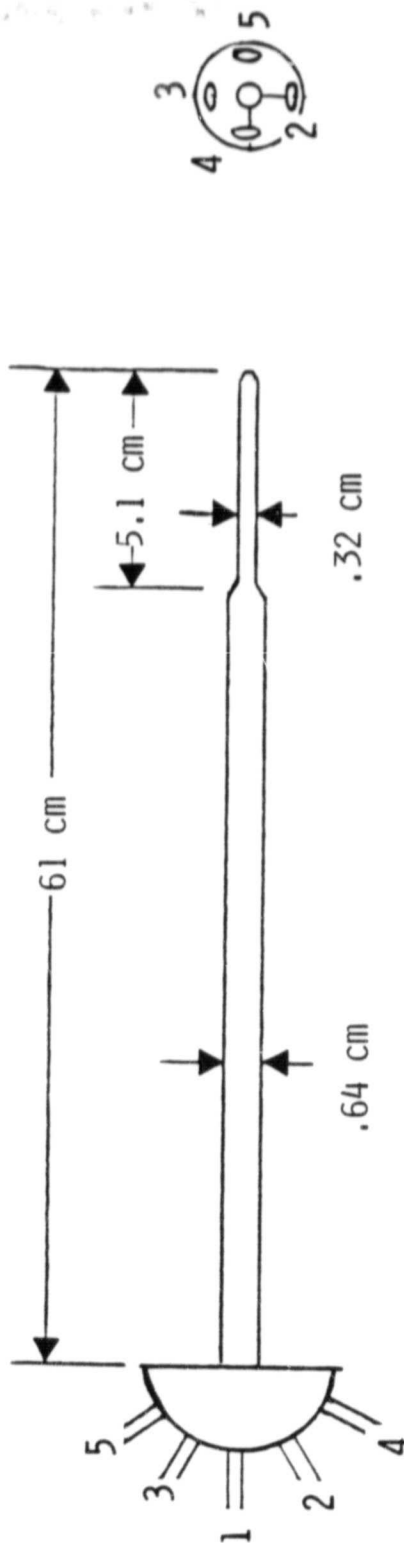


Fig. 7 - Yawhead Probe Used for Jet
Trajectory Measurements.

ORIGINAL PAGE IS
OF POOR QUALITY

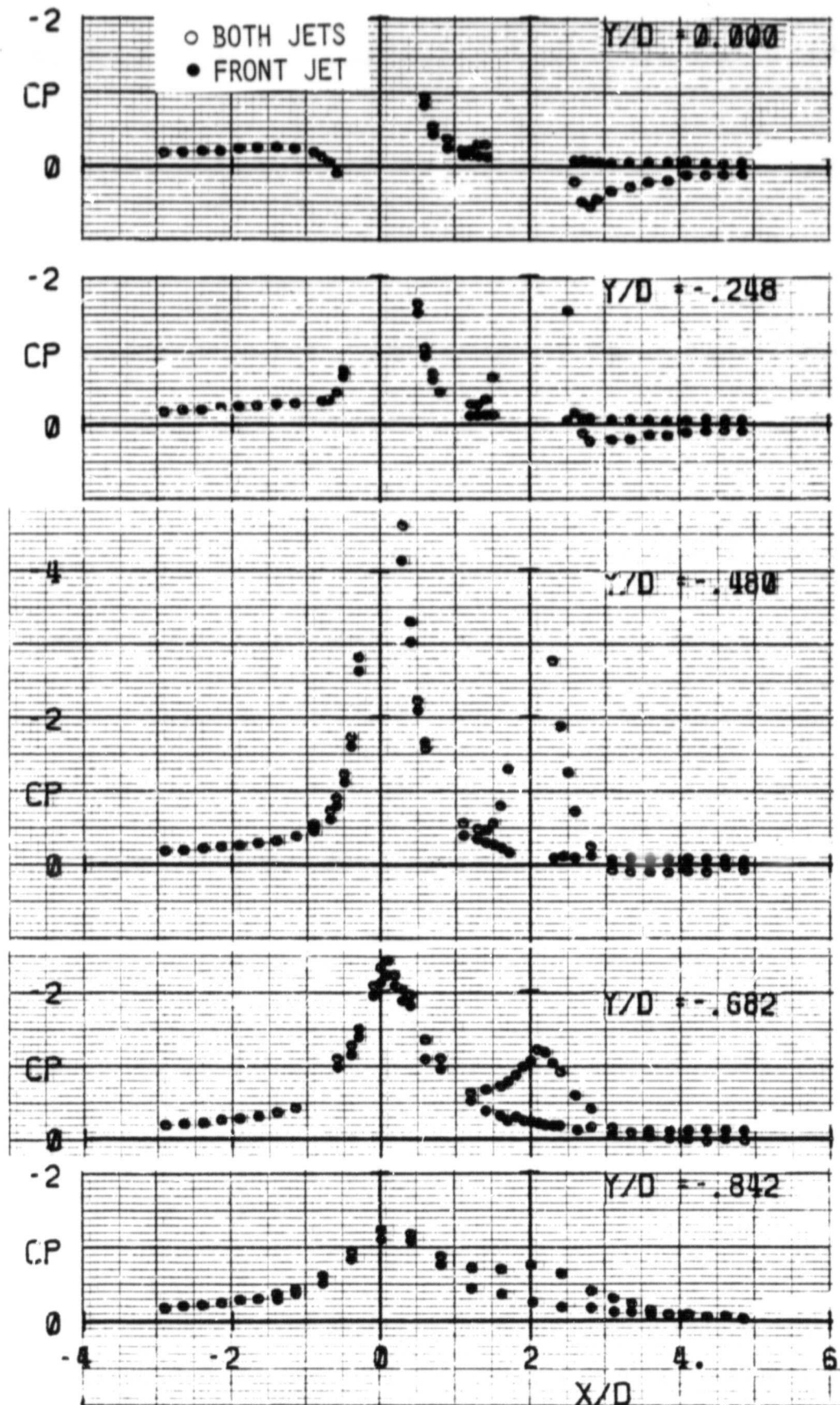


Fig. 8 - Surface Pressure Distribution
(ΔC_p): Body of Revolution
Model, 90 deg., $R = 7.7$, $S/D = 2$ and Contoured Exit.

ORIGINAL PAGE IS
OF POOR QUALITY

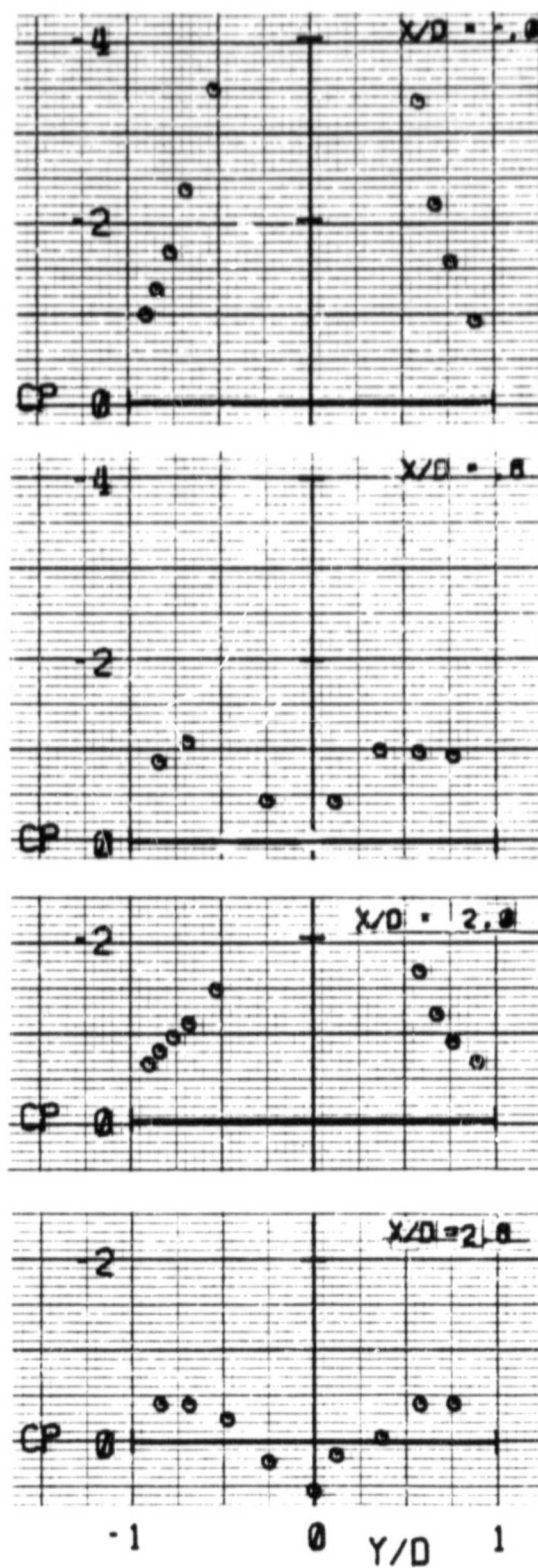


Fig. 9 - Transverse Plot of Surface Pressure Distribution on the Body of Revolution with 90 deg., $R = 7.7$, $S/D = 2$ and Contoured Exit.

ORIGINAL PAGE IS
OF POOR QUALITY

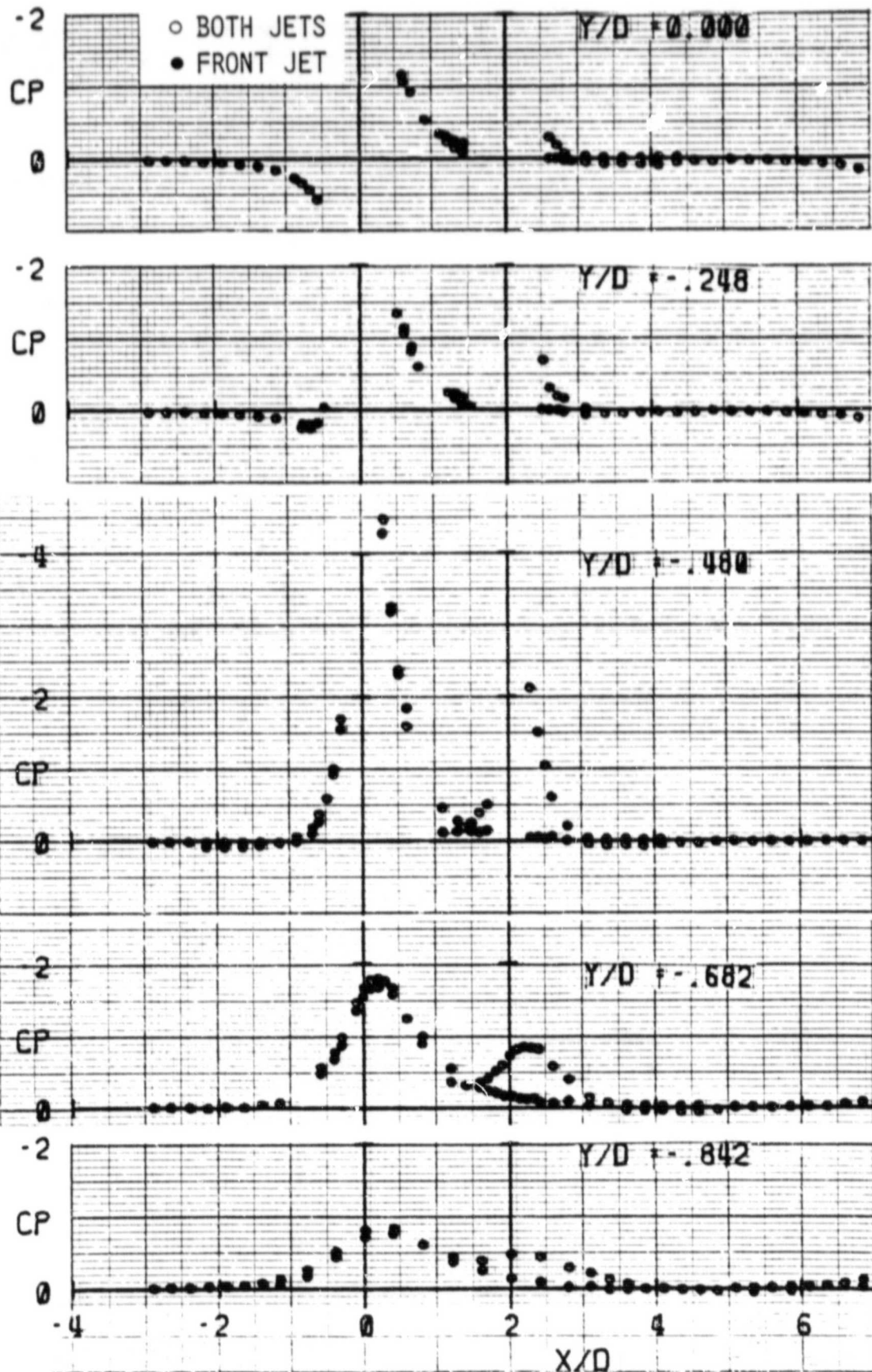


Fig. 10 - Surface Pressure Distribution
(ΔC_p): Body of Revolution
Model, 90 deg., $R = 3.2$, $S/D =$
2 and Contoured Exit.

ORIGINAL PAGE IS
OF POOR QUALITY

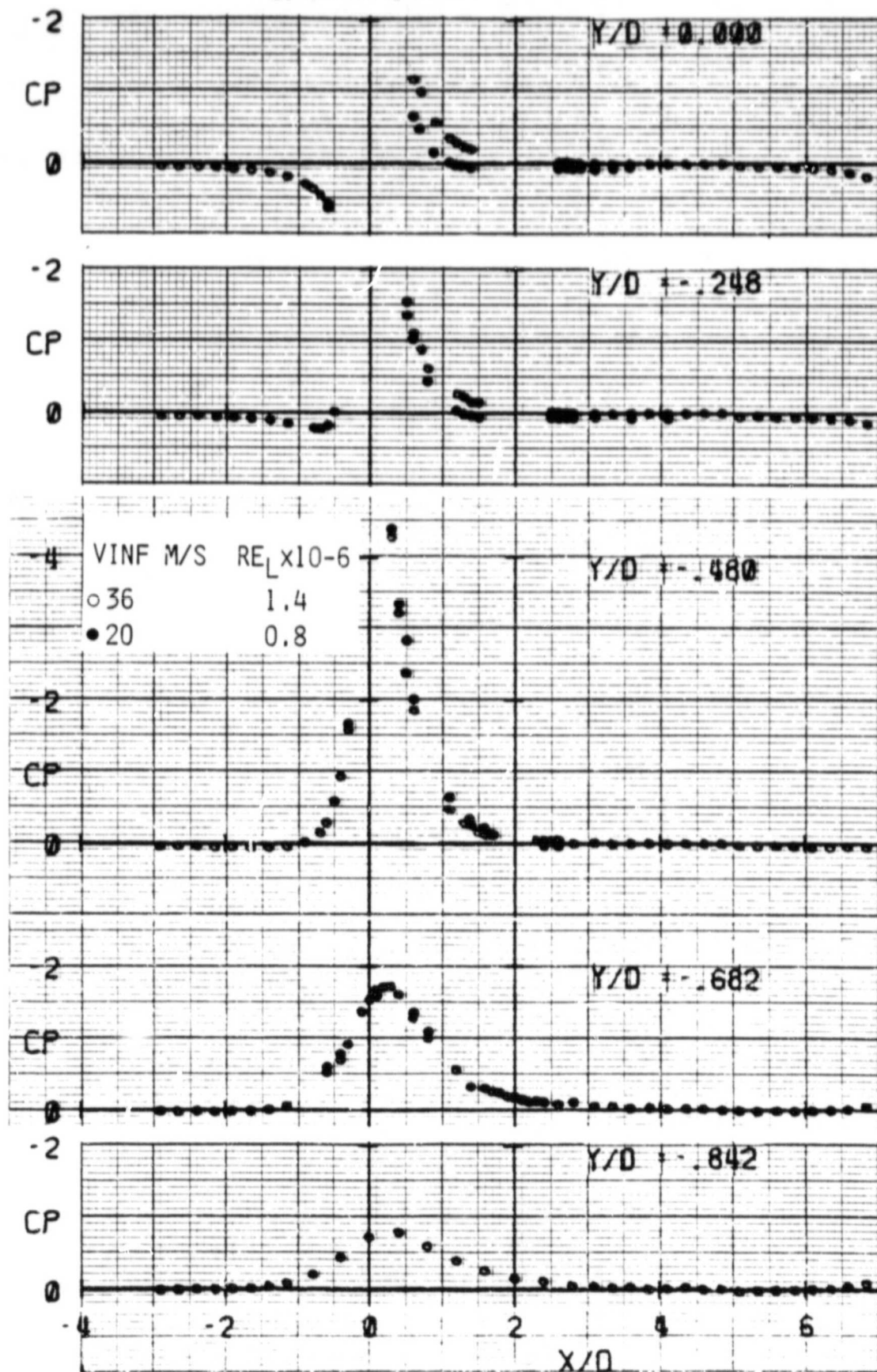


Fig. 11 - Comparison of Surface Pressure Distribution at the Same $R = 3.2$, but Two Different Re_L with 90 deg., $S/D = 2$ and Contoured Exit. Front Nozzle Only.

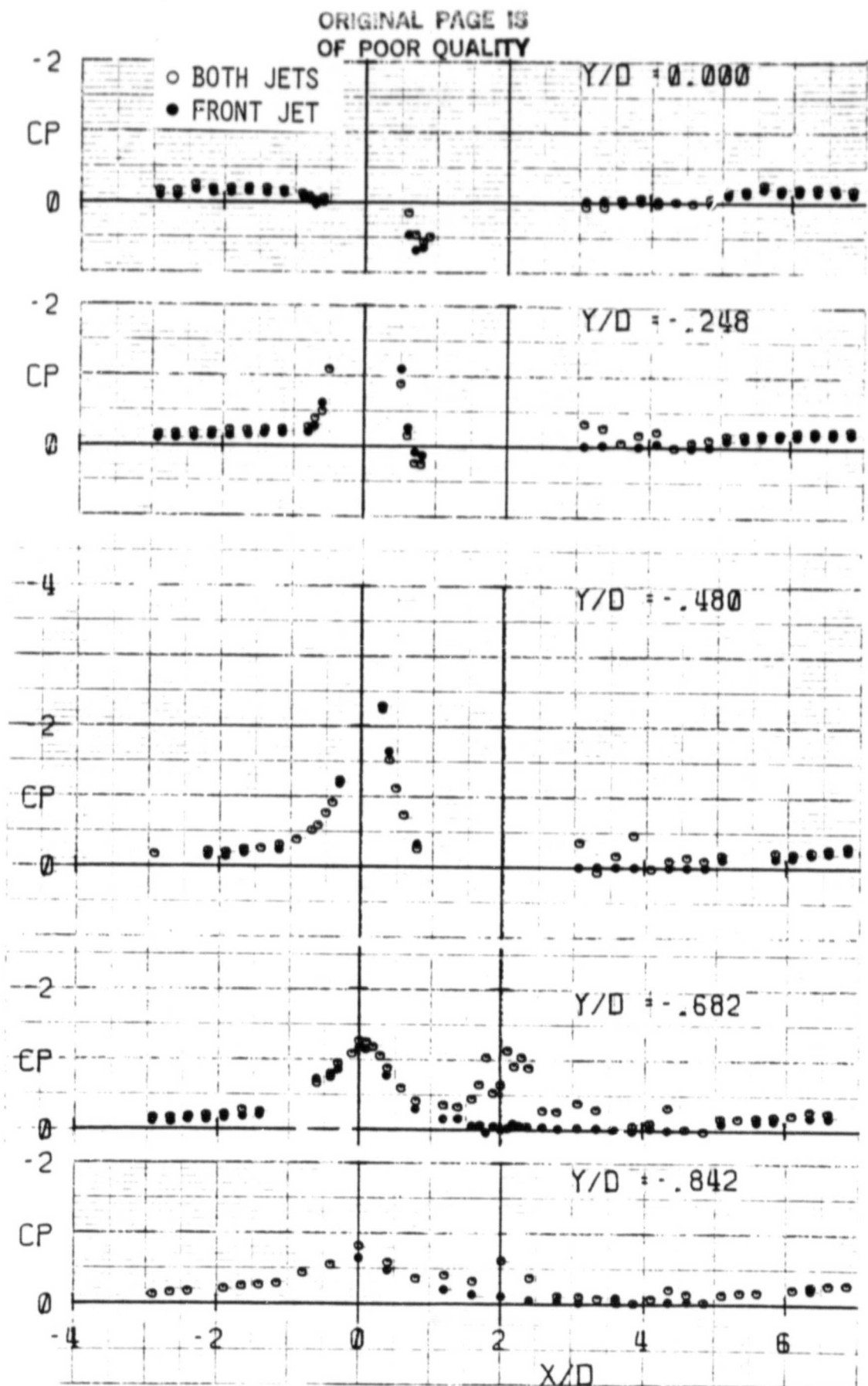


Fig. 12 - Surface Pressure Distribution
(ΔC_p): Body of Revolution
Model, 90 deg., $R = 8$, $S/D =$
2 and Flat Top Exit.

ORIGINAL PAGE IS
OF POOR QUALITY

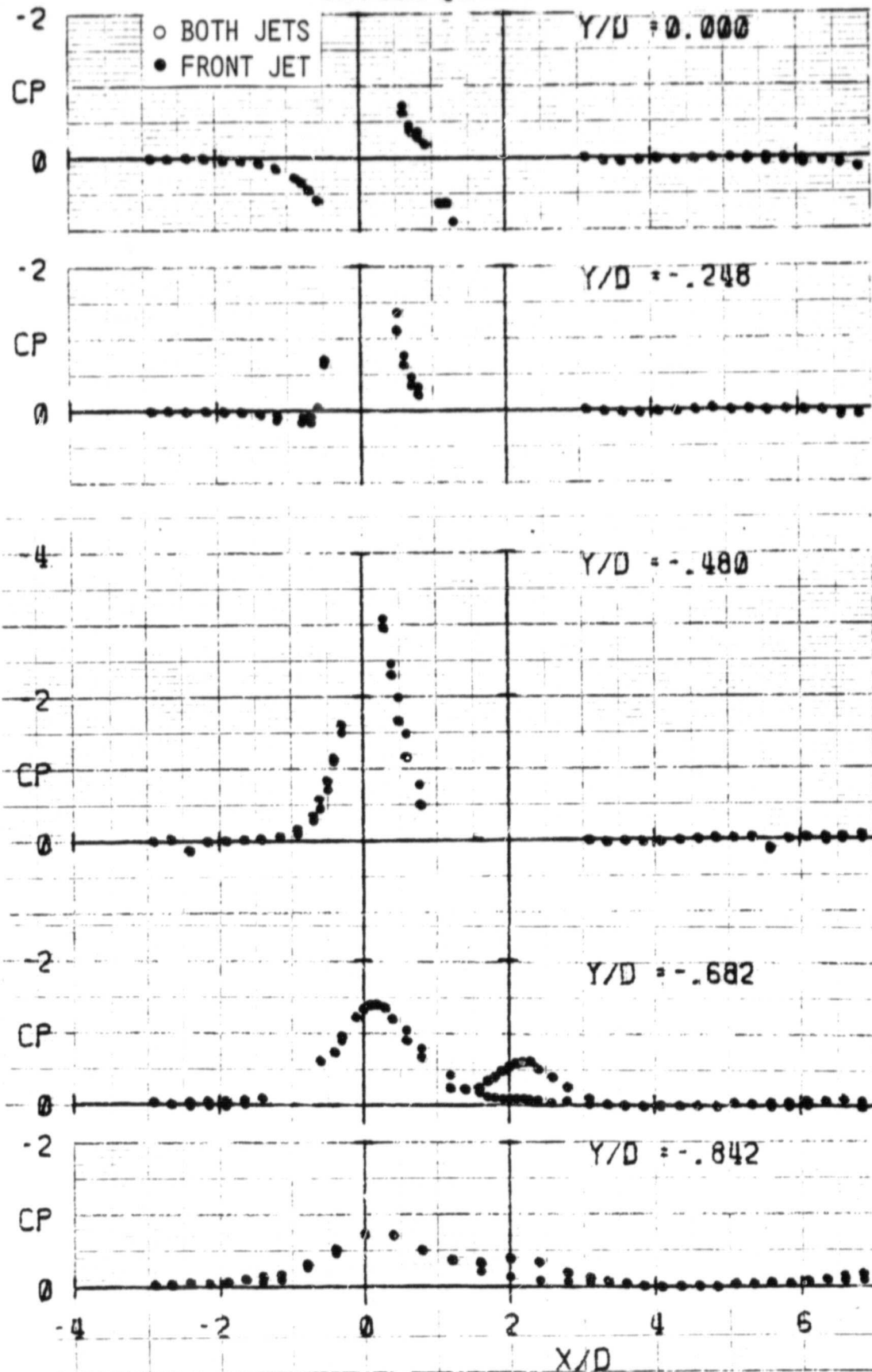


Fig. 13 - Surface Pressure Distribution
(ΔC_p): Body of Revolution
Model, 90 deg., $R = 3.3$, $S/D = 2$ and Flat Top Exit.

ORIGINAL PAGE IS
OF POOR QUALITY

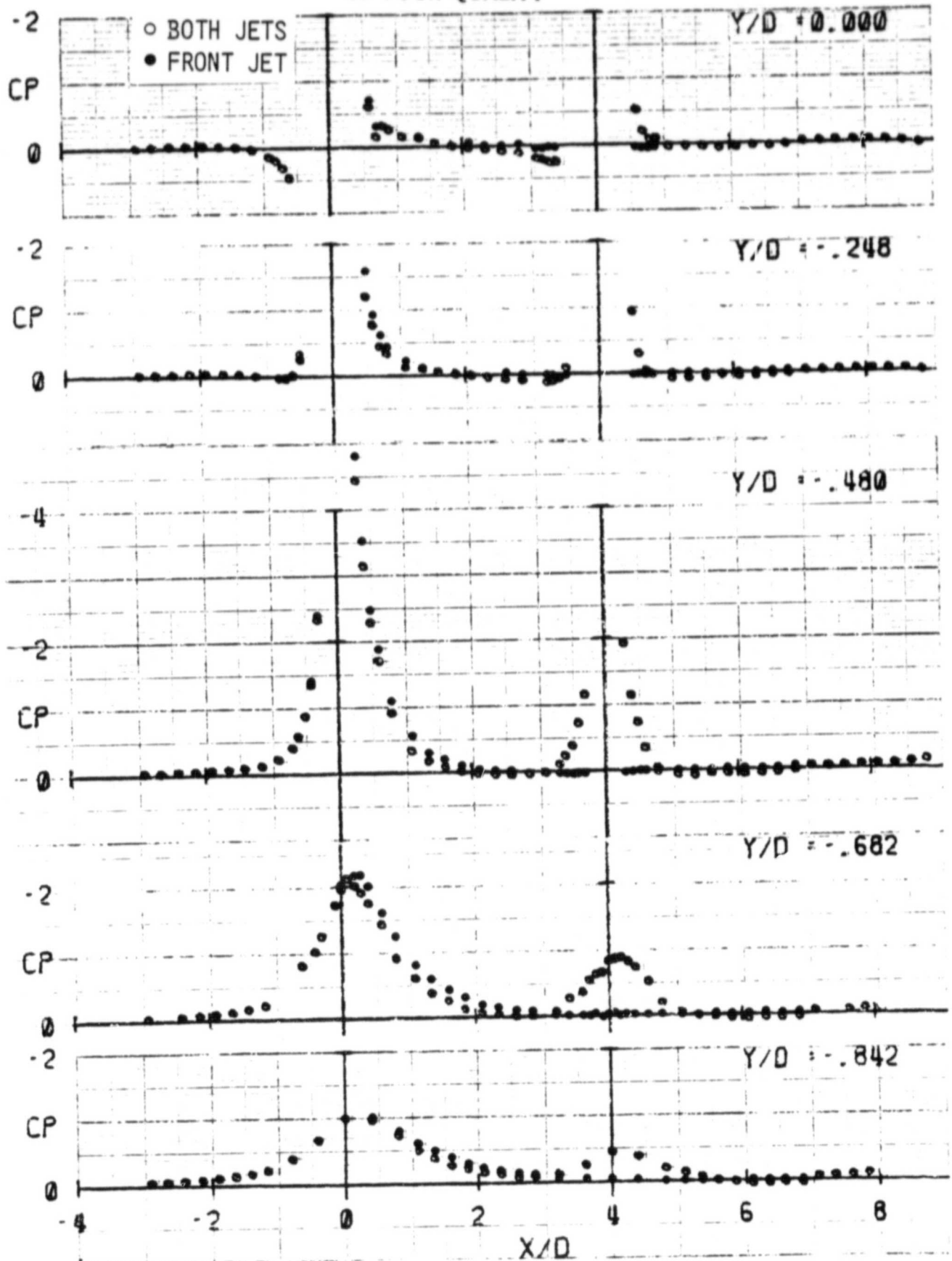


Fig. 14 - Surface Pressure Distribution
(ΔC_p): Body of Revolution
Model, 90 deg., $R = 4.7$, $S/D = 4$ and Contoured Exit.

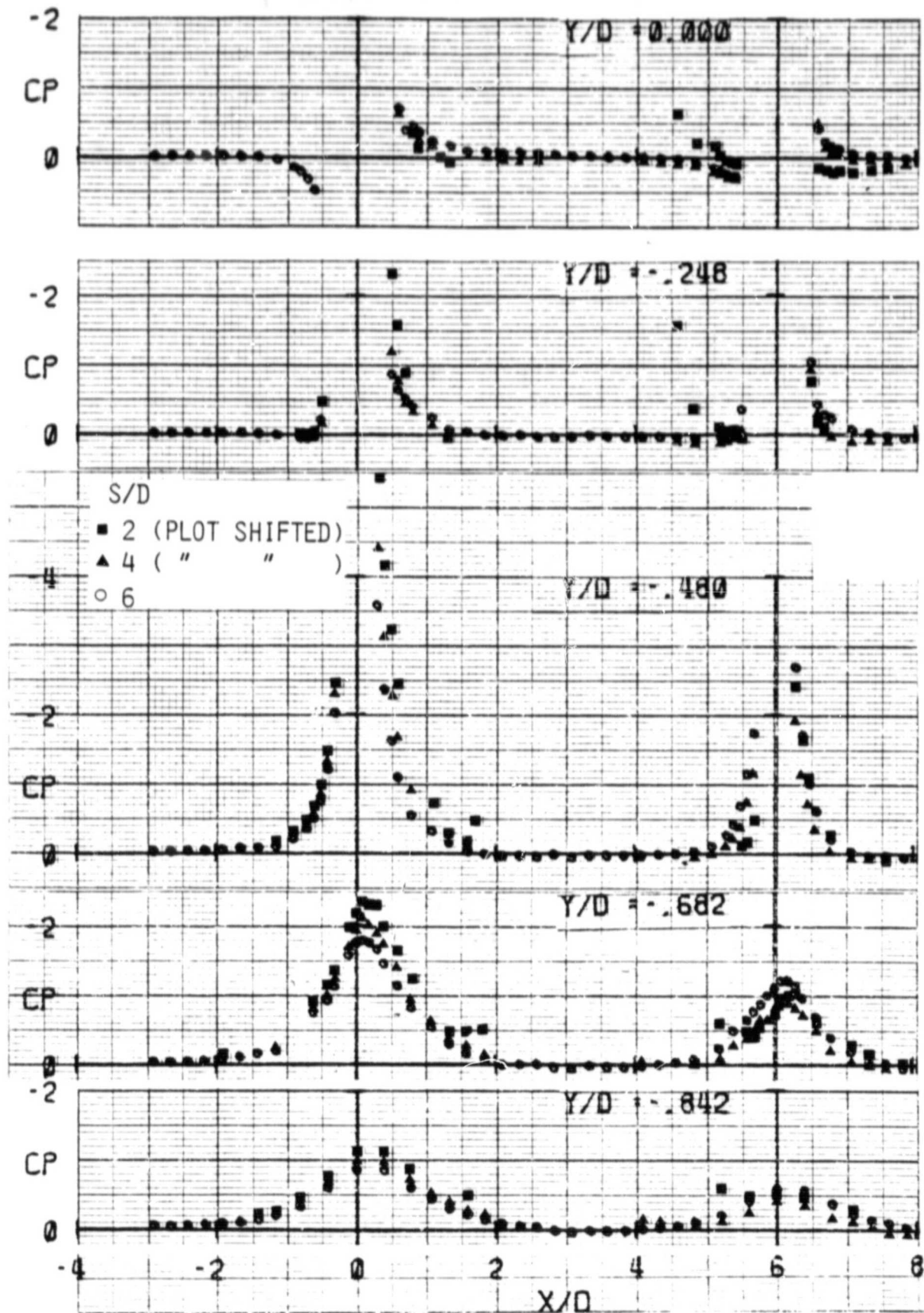


Fig. 15 - Surface Pressure Distribution
(ΔC_p): Body of Revolution
Model, 90 deg., $R = 4.7$, $S/D =$
2, 4 and 6 and Contoured Exit.

ORIGINAL PAGE IS
OF POOR QUALITY

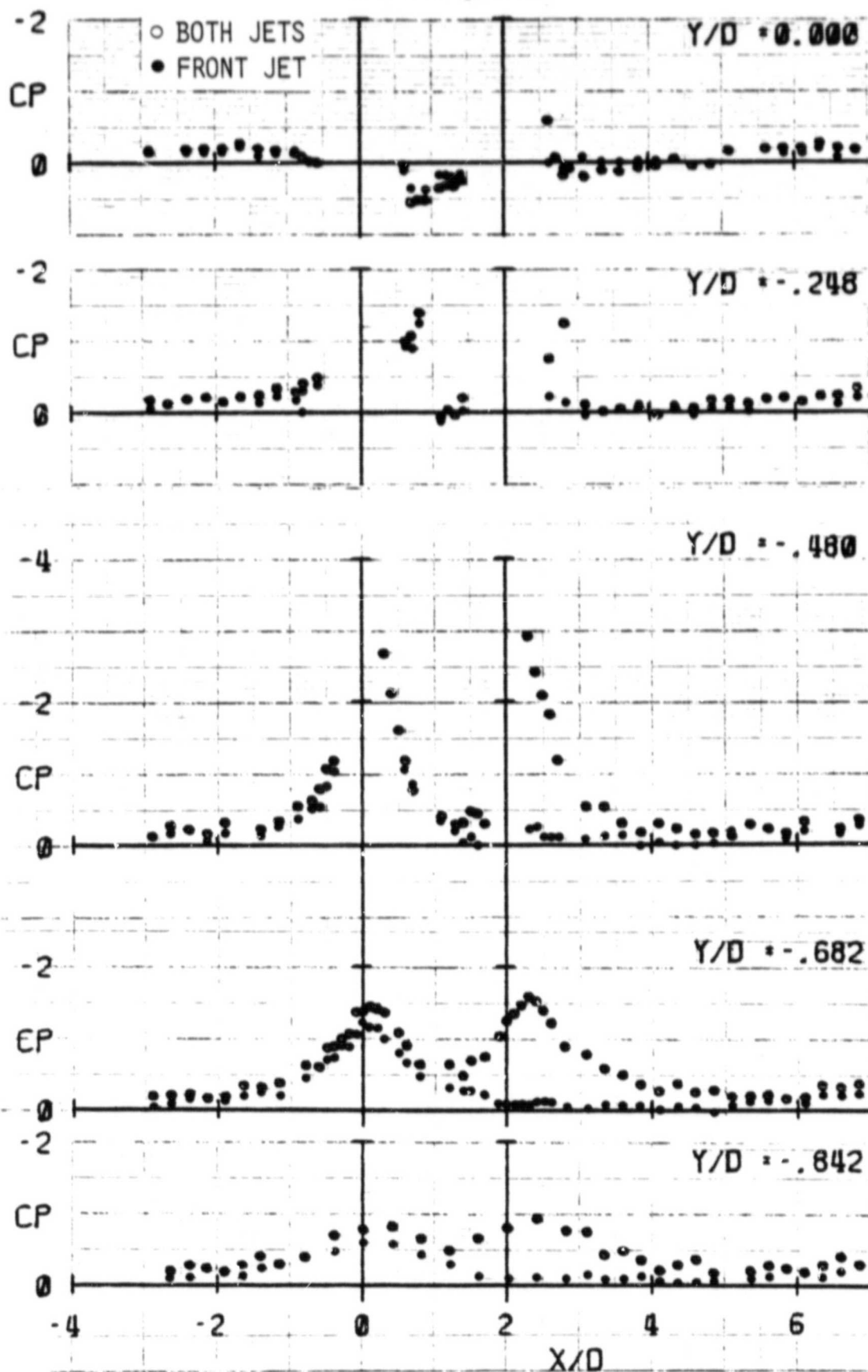


Fig. 16 - Surface Pressure Distribution
(ΔC_p): Body of Revolution
Model, 75 deg., $R = 8$, $S/D =$
2 and Flat Top Exit.

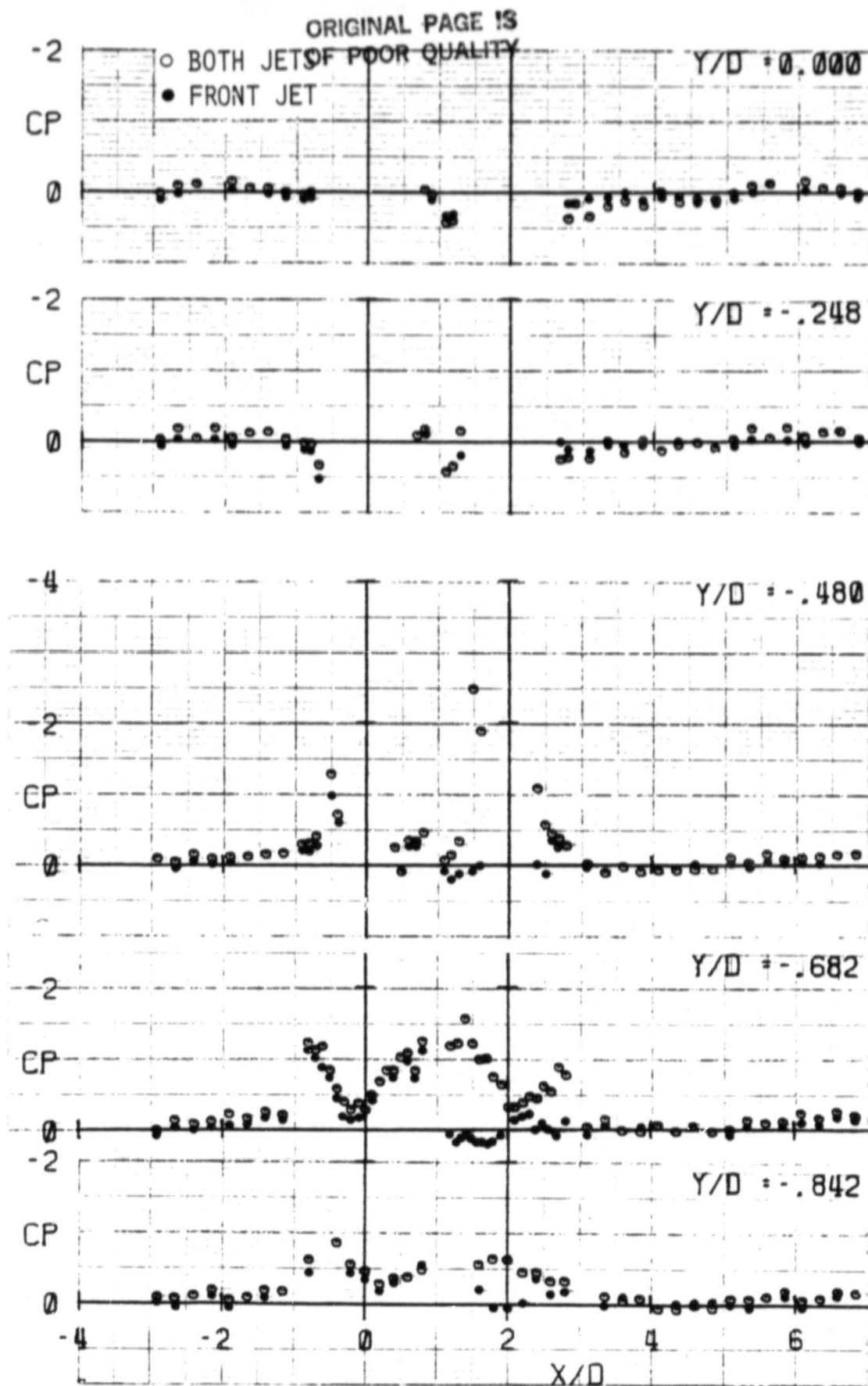


Fig. 17 - Surface Pressure Distribution
 (ΔC_p): Body of Revolution
 Model, 60 deg., $R = 8$, $S/D =$
 2 and Flat Top Exit.

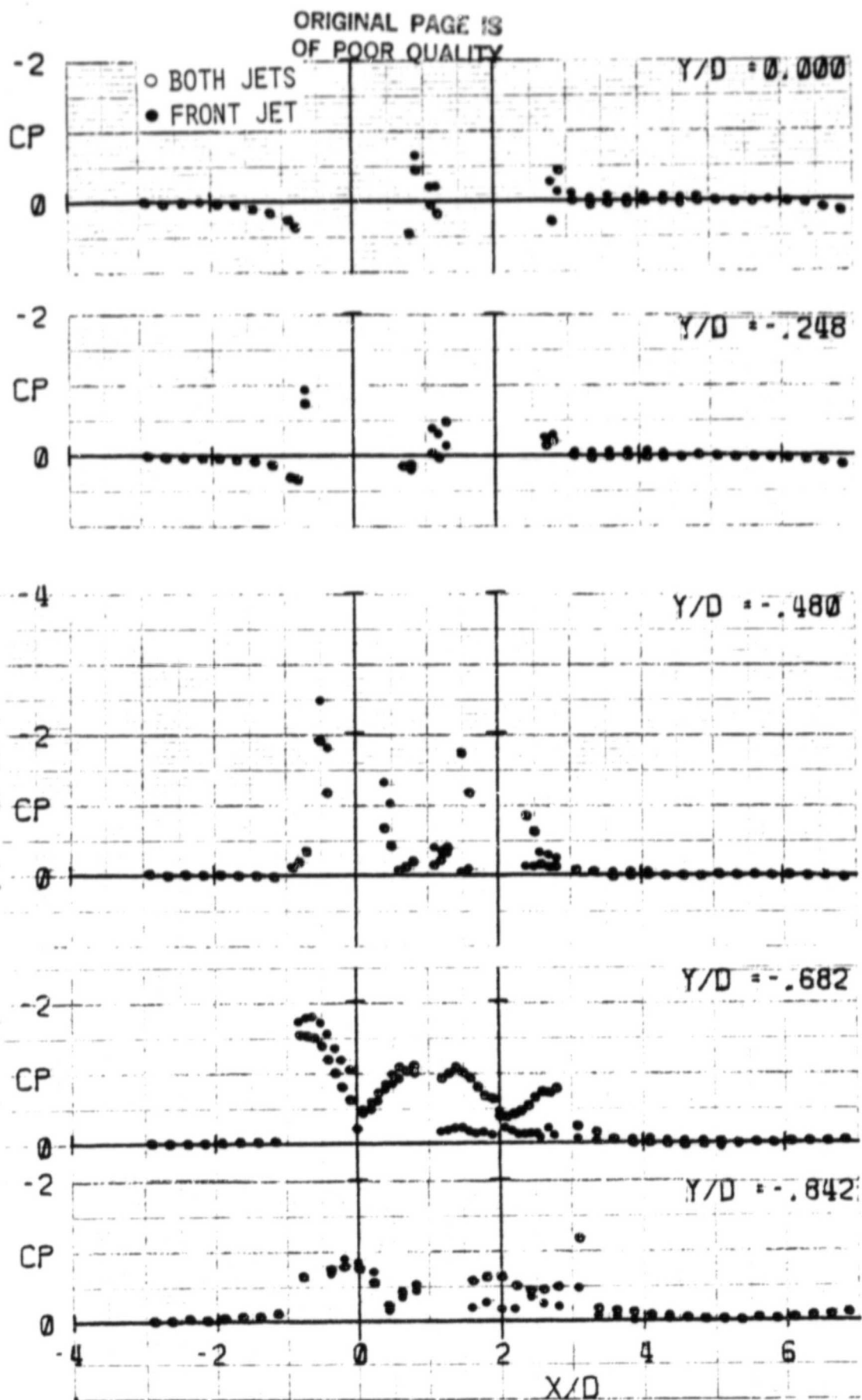


Fig. 18 - Surface Pressure Distribution (ΔC_p): Body of Revolution Model, 60 deg., $R = 4$, $S/D = 2$ and Flat Top Exit.

ORIGINAL PAGE IS
OF POOR QUALITY

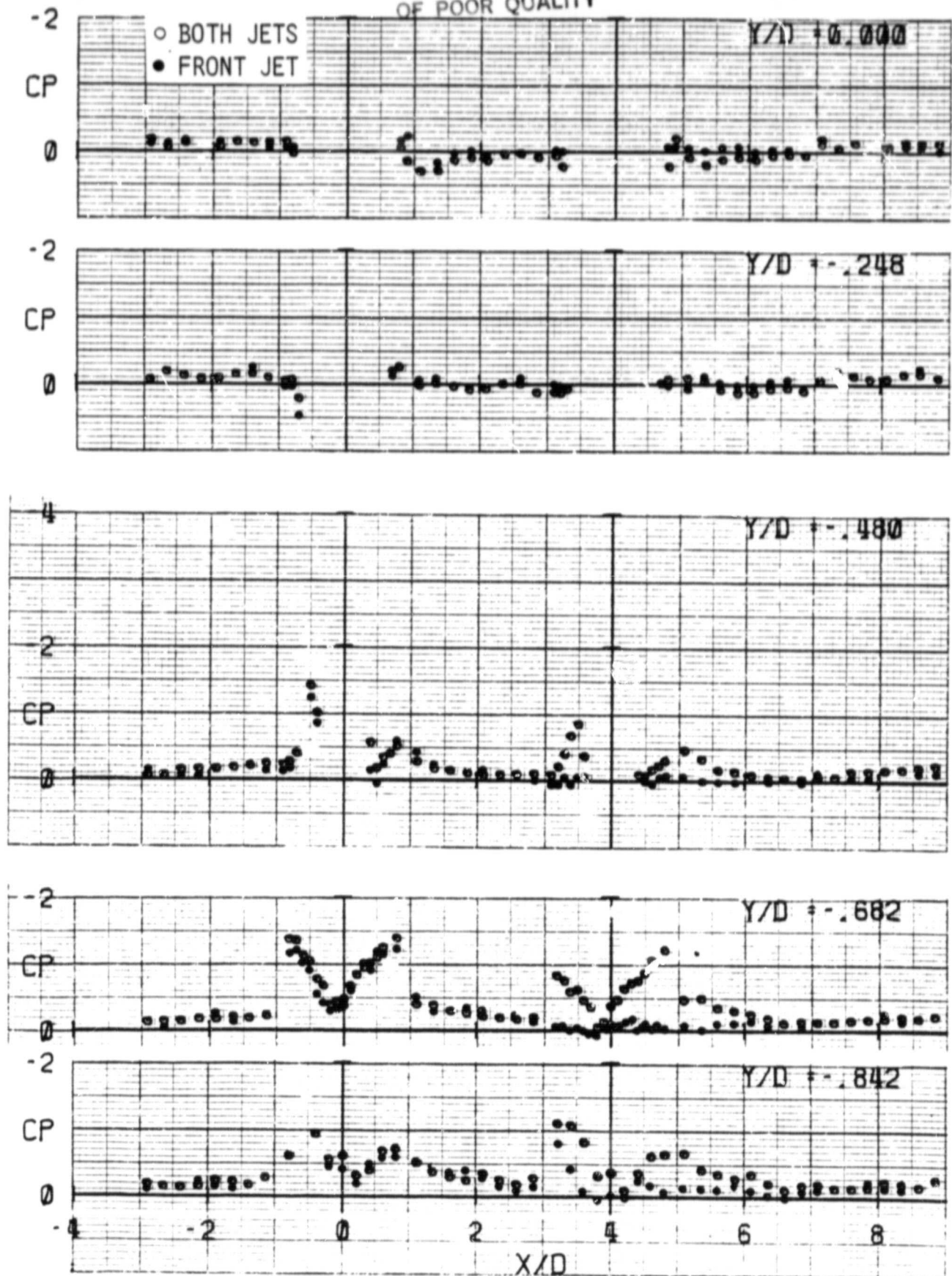


Fig. 19 - Surface Pressure Distribution
(ΔC_p): Body of Revolution
Model, 60 deg., $R = 8$, $S/D =$
4 and Flat Top Exit.

ORIGINAL PAGE IS
OF POOR QUALITY

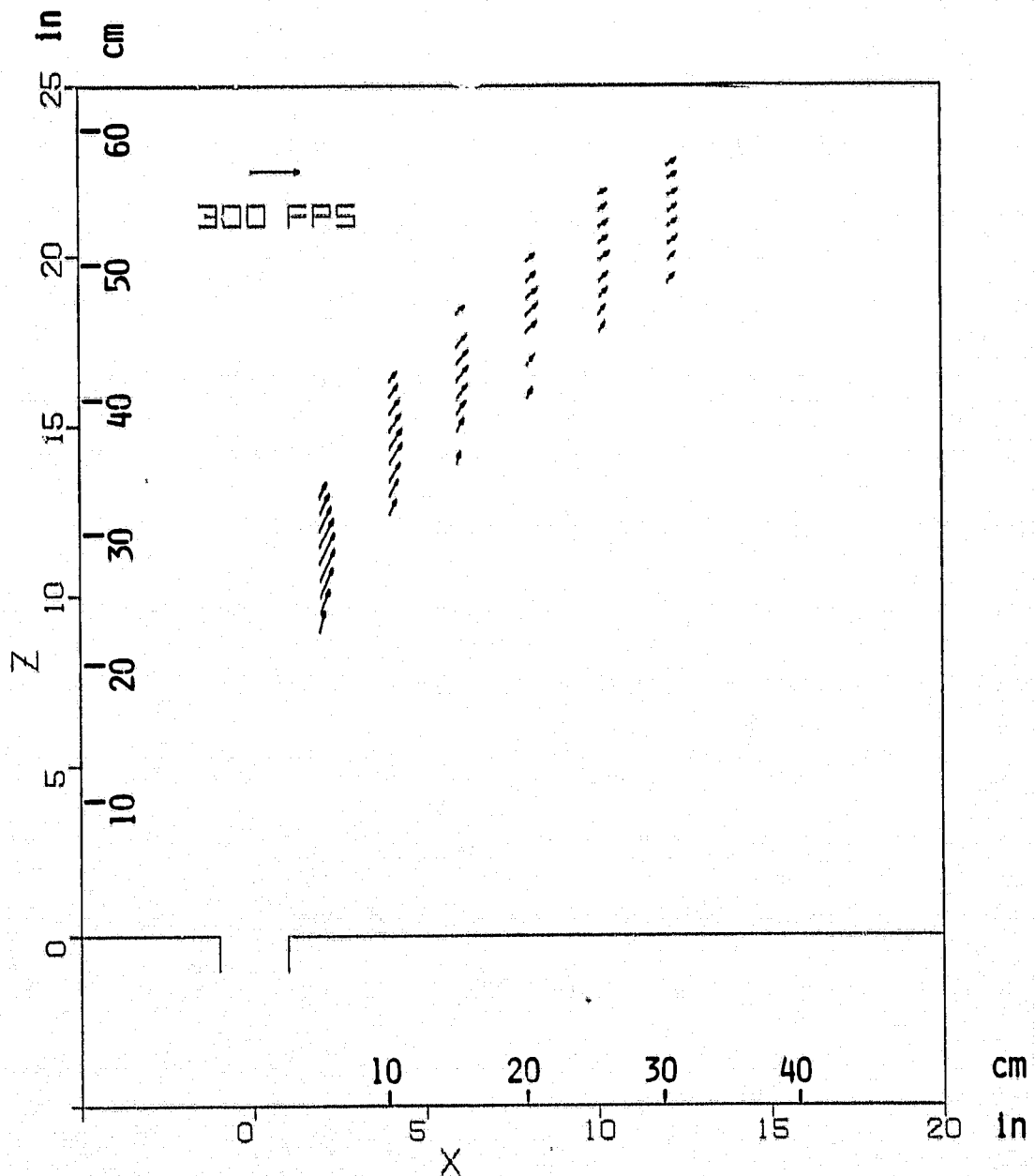


Fig. 20 - Velocity Vector Plot in the
Jet: Body of Revolution Model,
90 deg., R = 6.5. Front
Nozzle Only.

ORIGINAL PAGE IS
OF POOR QUALITY

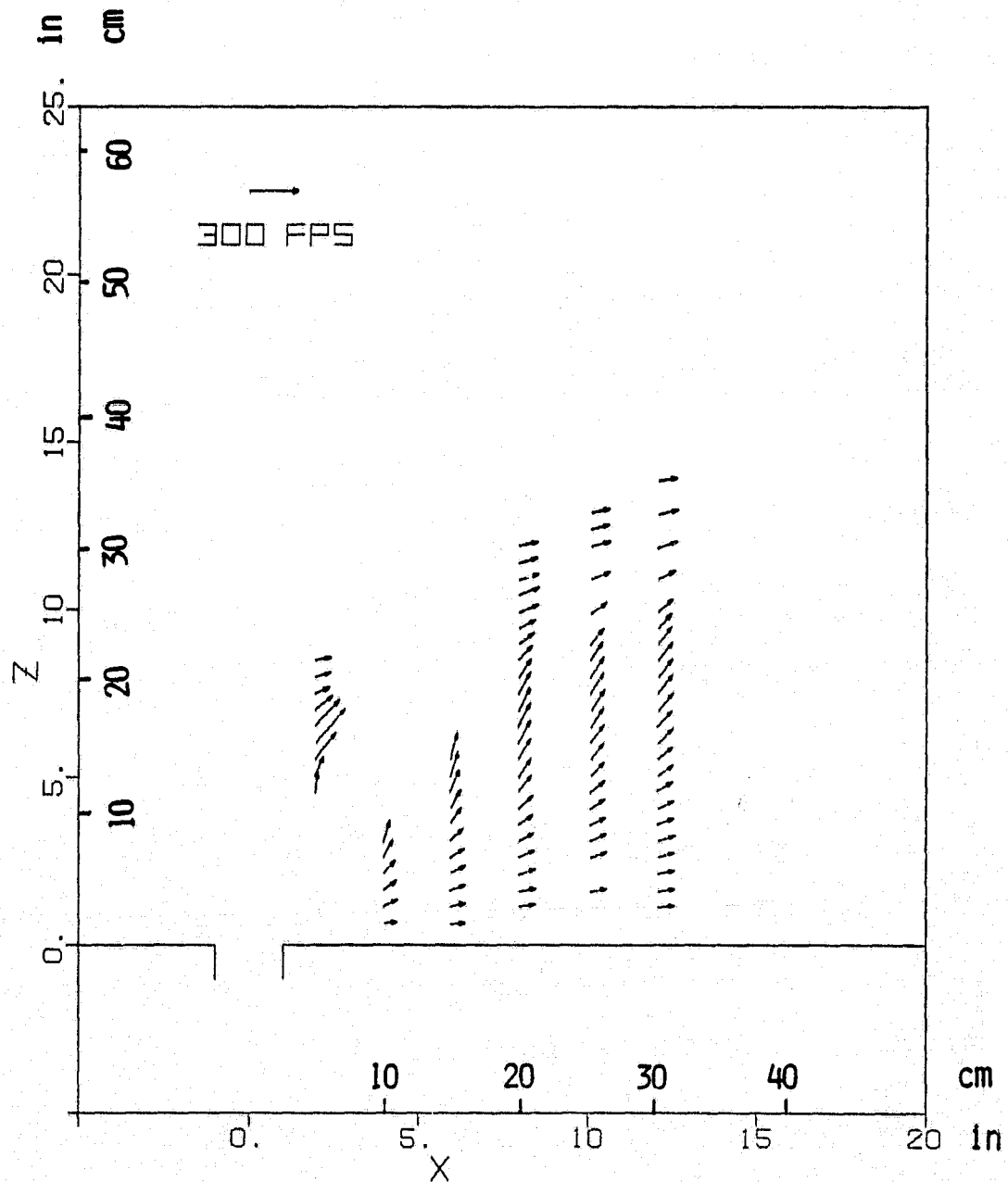


Fig. 21 - Velocity Vector Plot in the
Jet: Body of Revolution Model,
90 deg., $R = 3.2$. Front
Nozzle Only.

ORIGINAL PAGE IS
OF POOR QUALITY

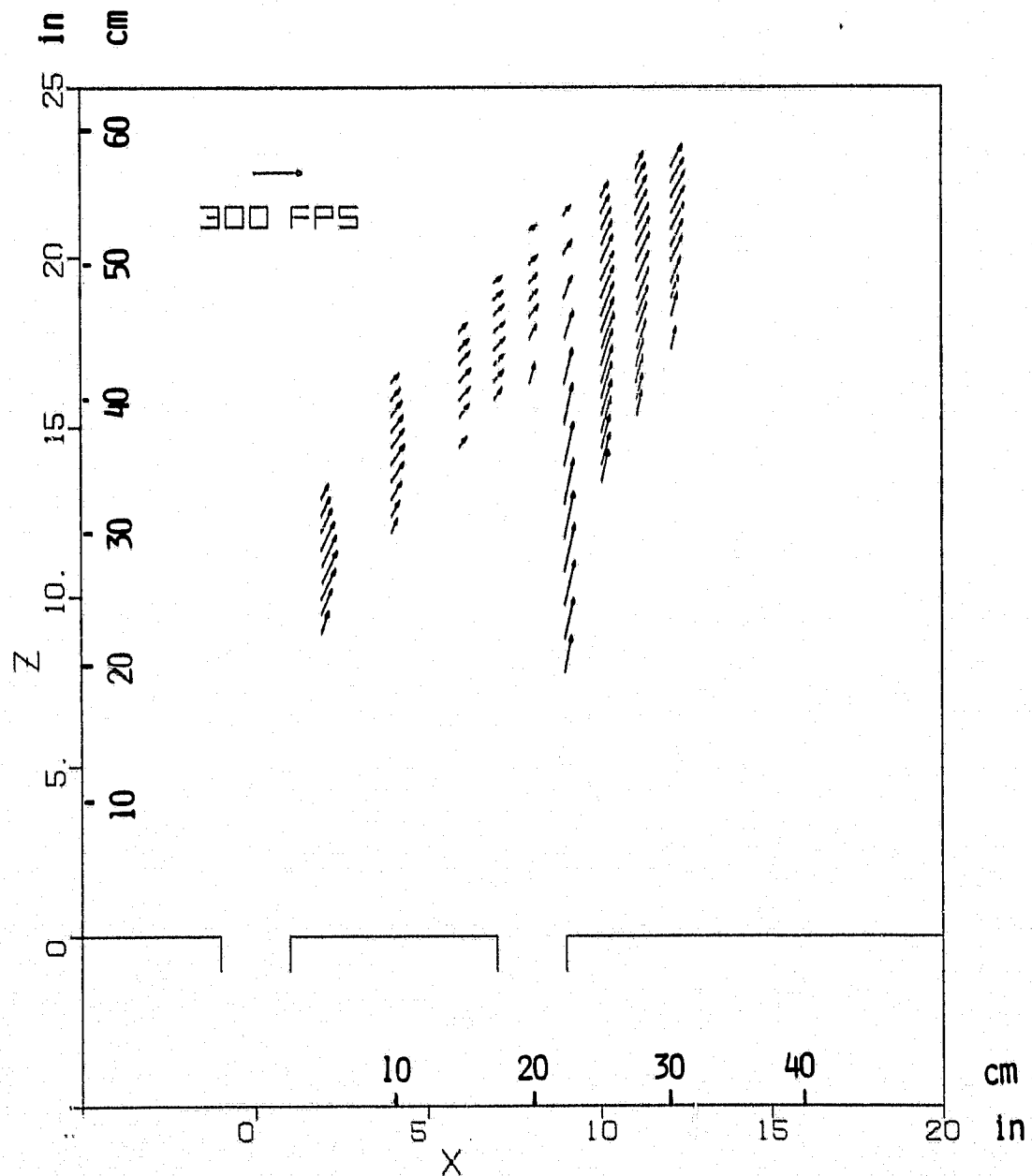


Fig. 22 - Velocity Vector Plot in the
Flowfield: Body of Revolution
Model, 90 deg., $R = 6.5$,
 $S/D = 4$.

ORIGINAL PAGE 13
OF POOR QUALITY

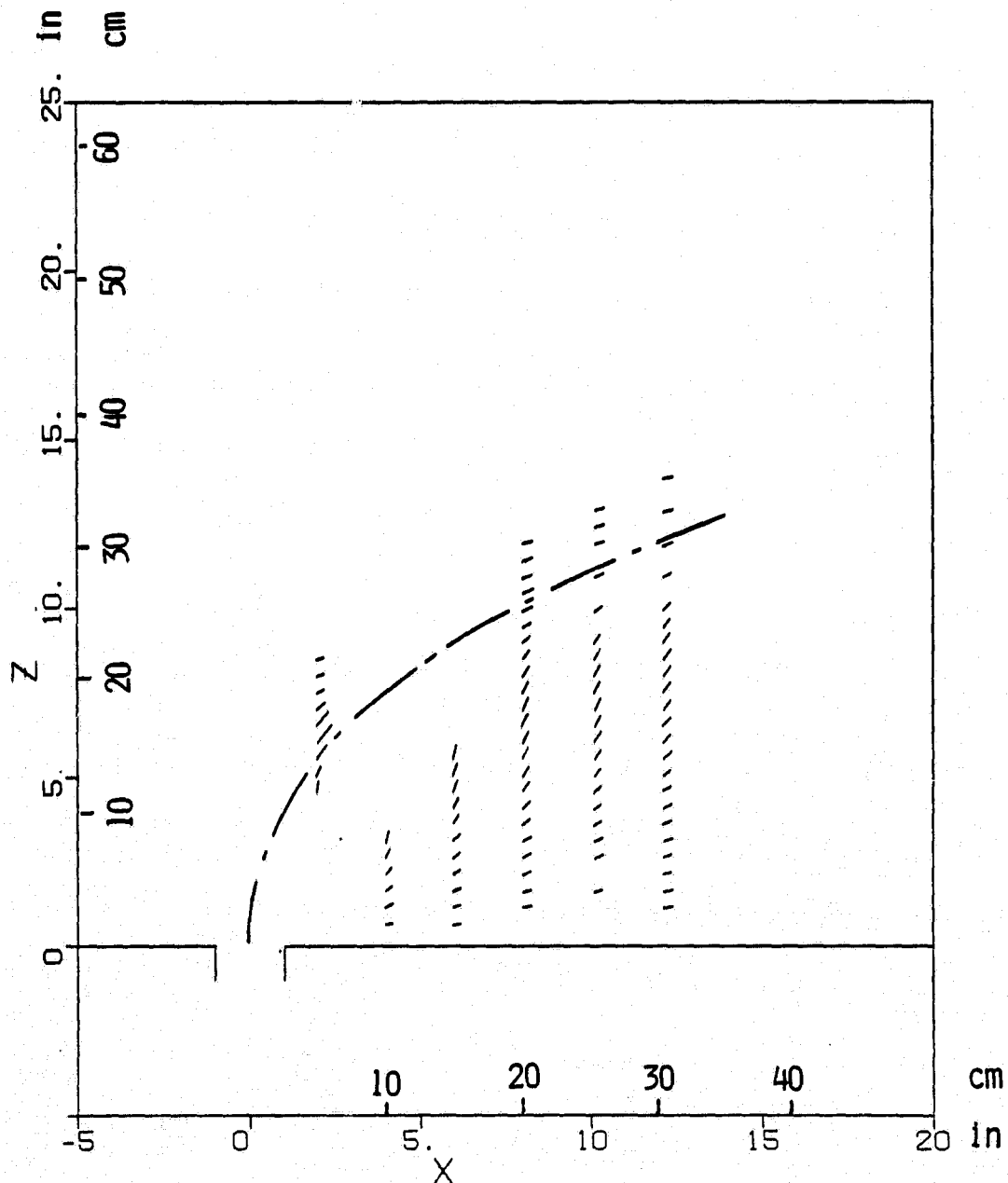


Fig. 23 - Comparison of Trajectory
Prediction with Analysis of
Ref. (28) and Velocity Vector
Data: 90 deg., $R = 3.2$.
Front Nozzle Only.

ORIGINAL PAGE IS
OF POOR QUALITY

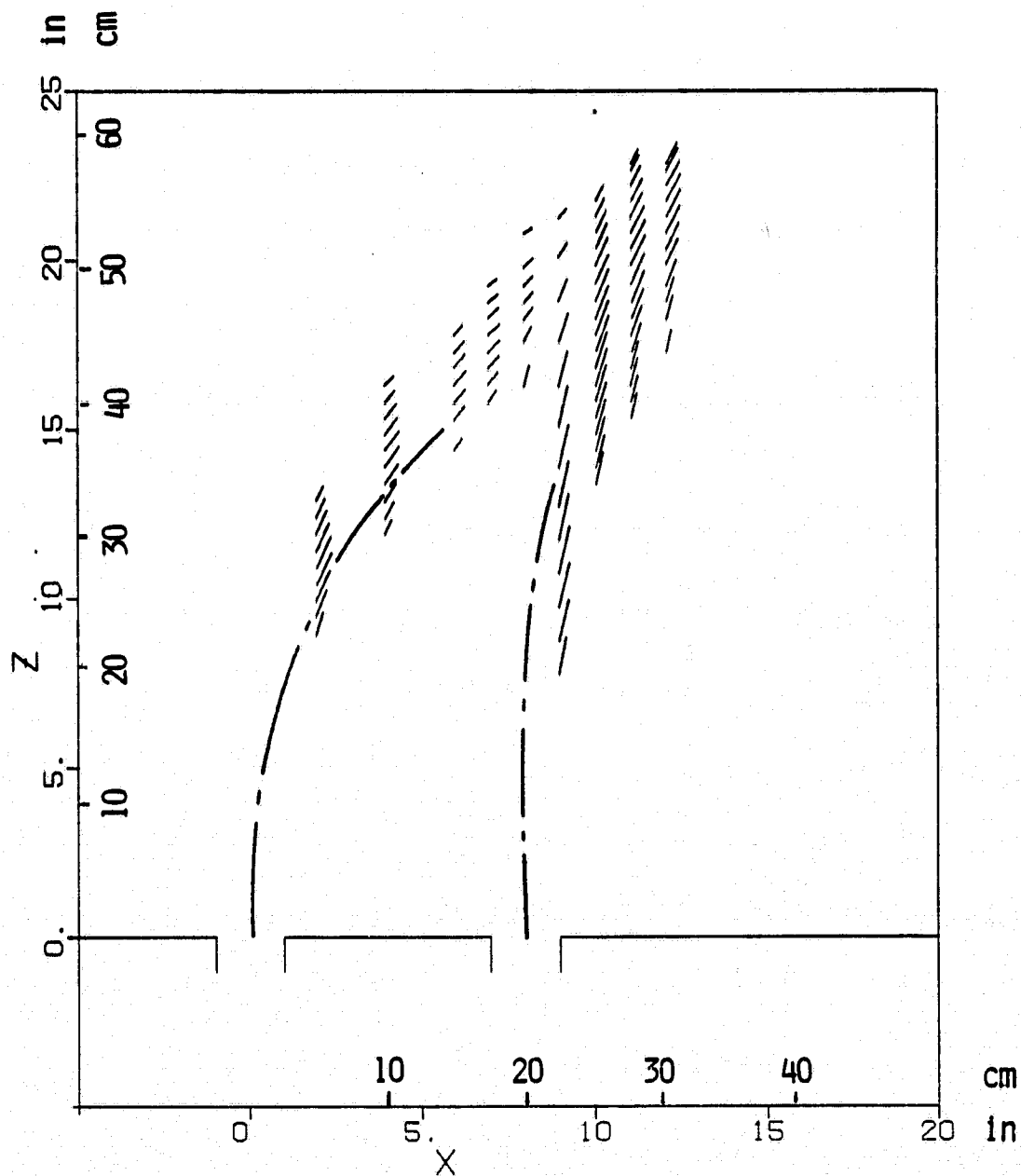


Fig. 24 - Comparison of Trajectory
Prediction with Analysis of
Ref. (28) and Velocity Vector
Data: 90 deg., $R = 6.5$,
 $S/D = 4$.

ORIGINAL PAGE 13
OF POOR QUALITY

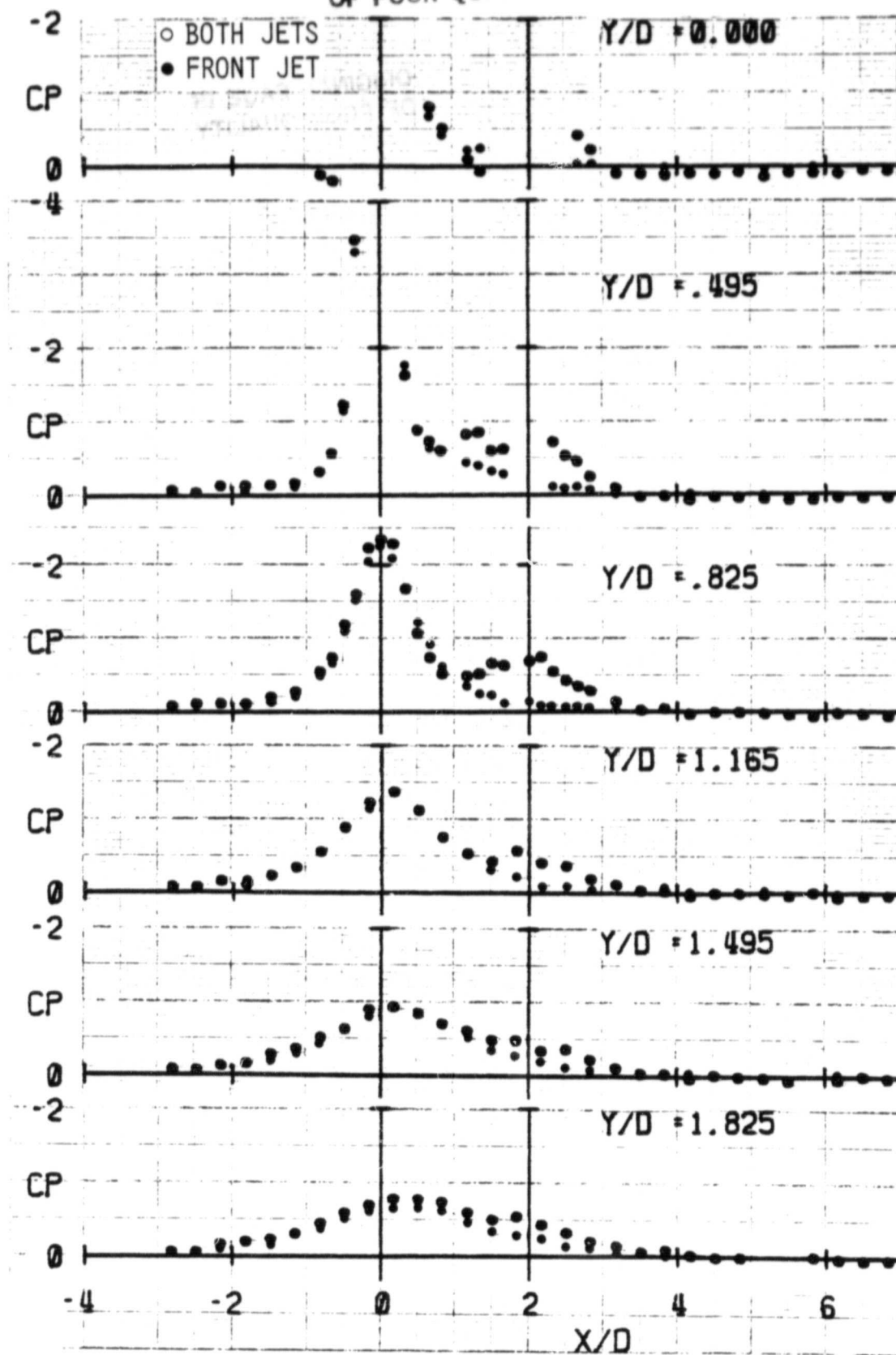


Fig. 25 - Surface Pressure Distribution
(ΔC_p): Flat Plate Model,
90 deg., $R = 6$, $S/D = 2$.

ORIGINAL PAGE 13
OF POOR QUALITY

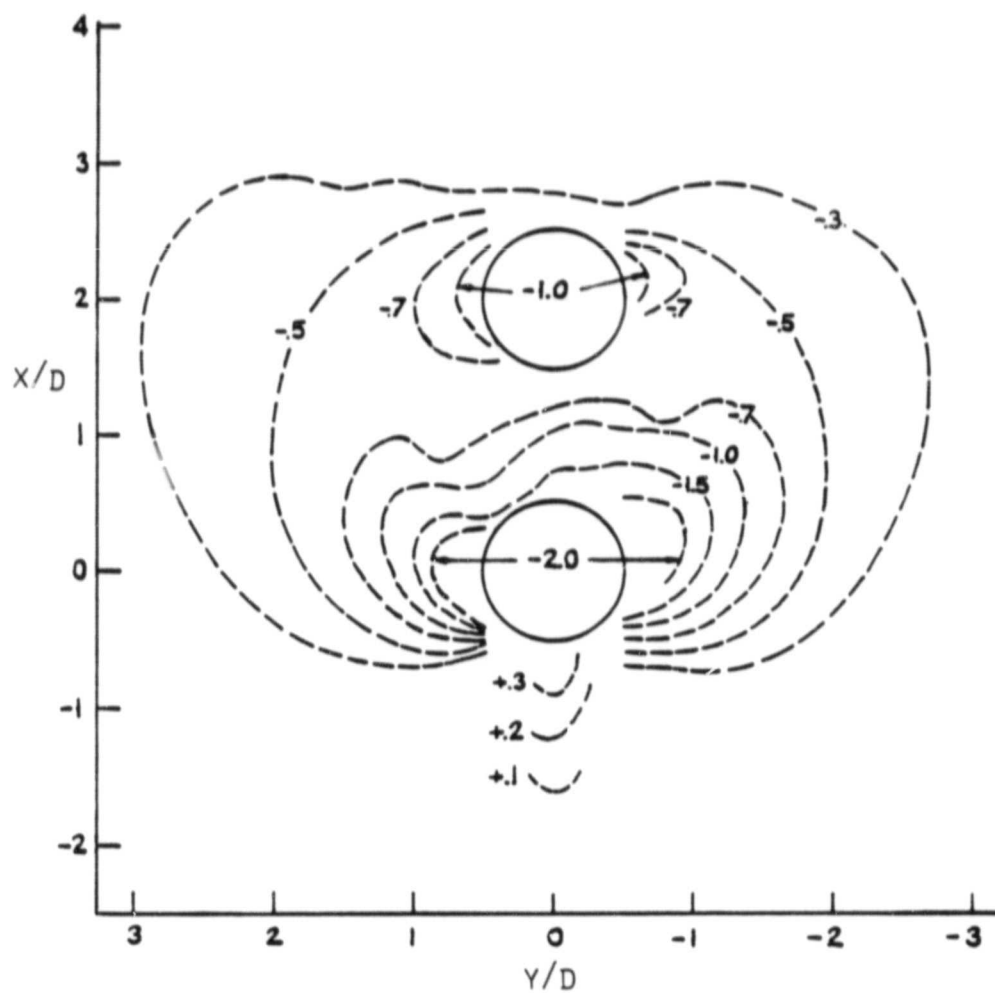


Fig. 26 - Isobar Map of ΔC_p : Flat
Plate with Both Jets,
90 deg., $R = 4$, $S/D = 2$.

ORIGINAL PAGE 13
OF POOR QUALITY

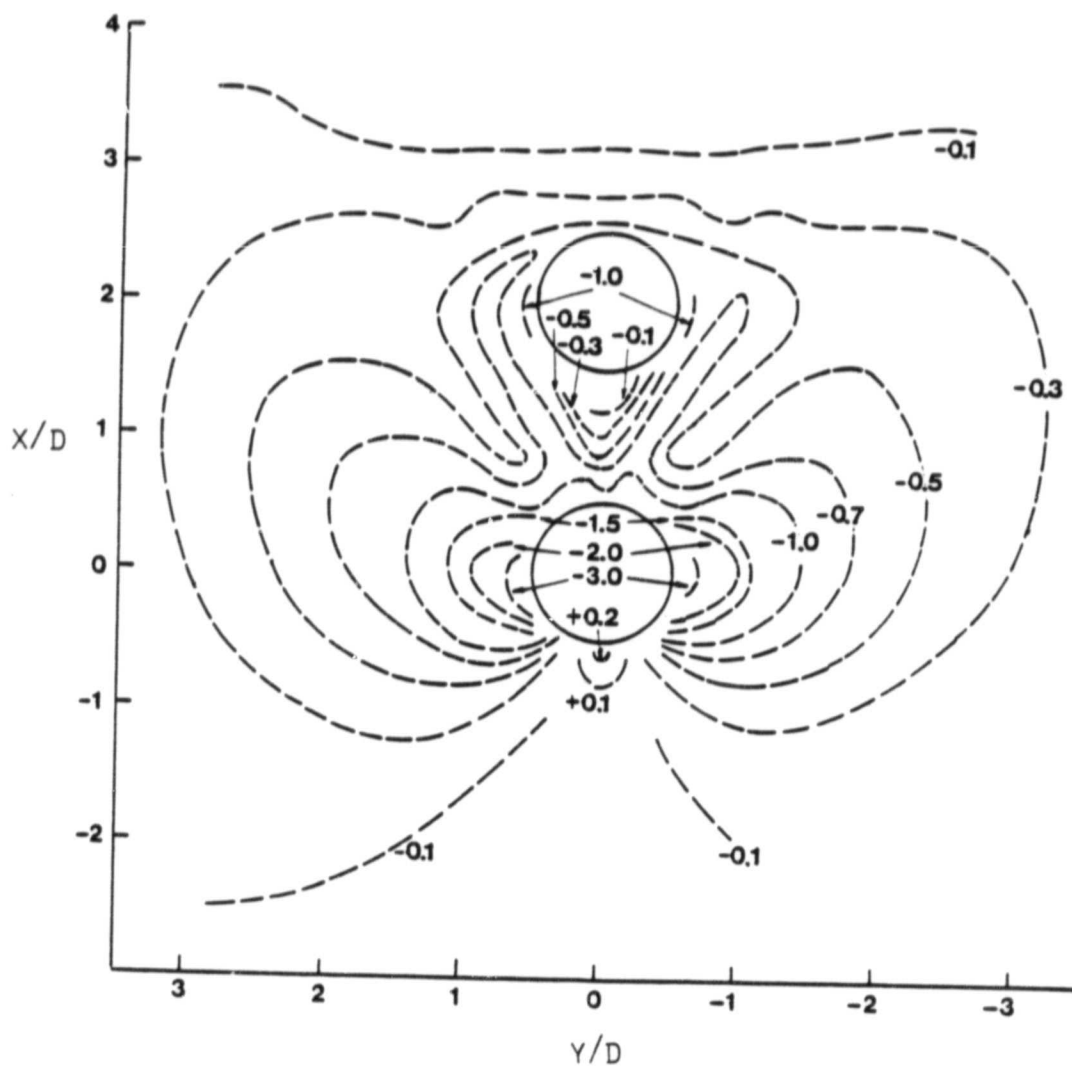


Fig. 27 - Isobar Map of ΔC_p : Flat
Plate with Both Jets,
90 deg., $R = 6$, $S/D = 2$.

ORIGINAL PAGE 13
OF POOR QUALITY

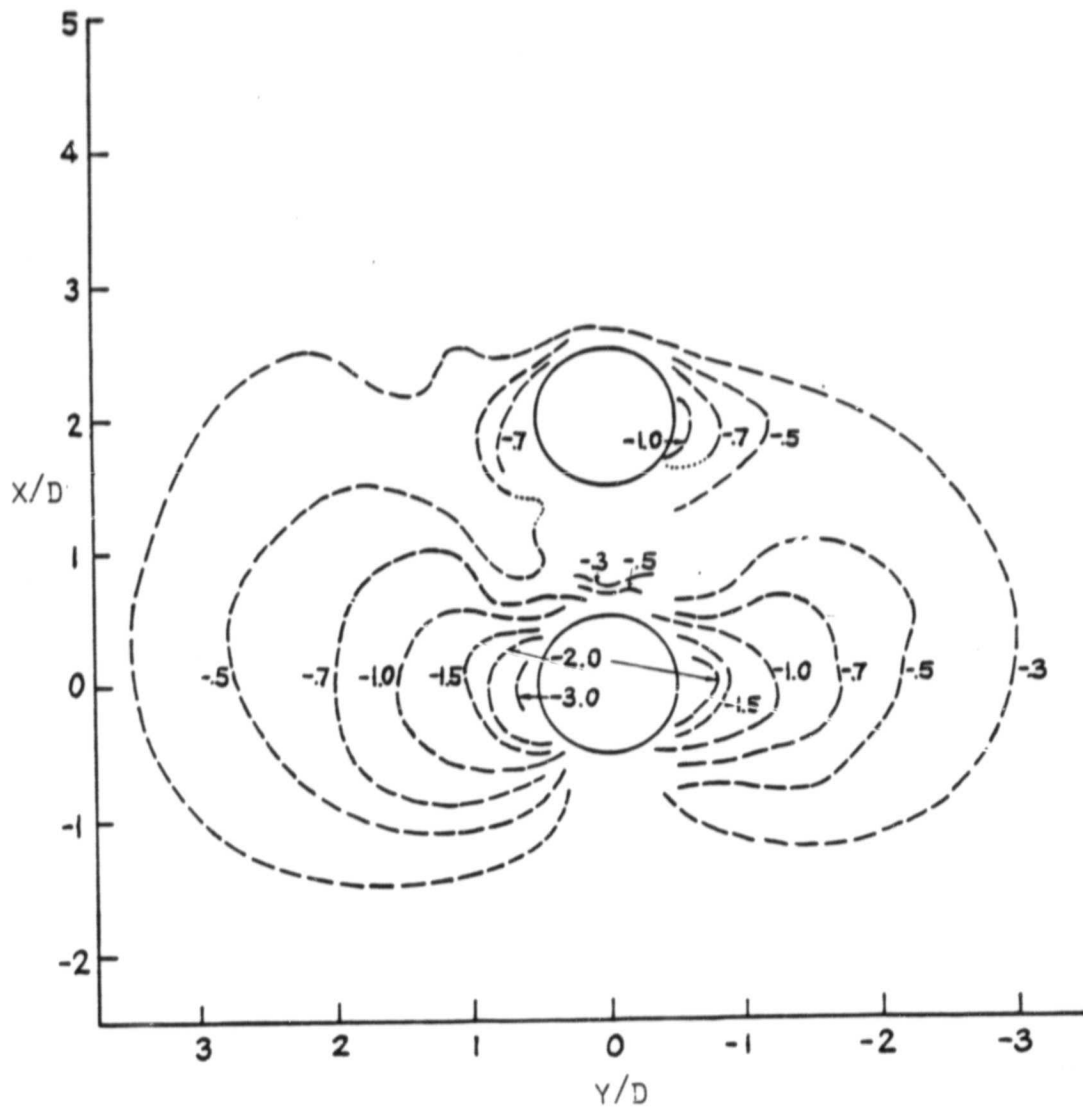


Fig. 28 - Isobar Map of ΔC_p : Flat
Plate with Both Jets,
90 deg., $R = 8$, $S/D = 2$.

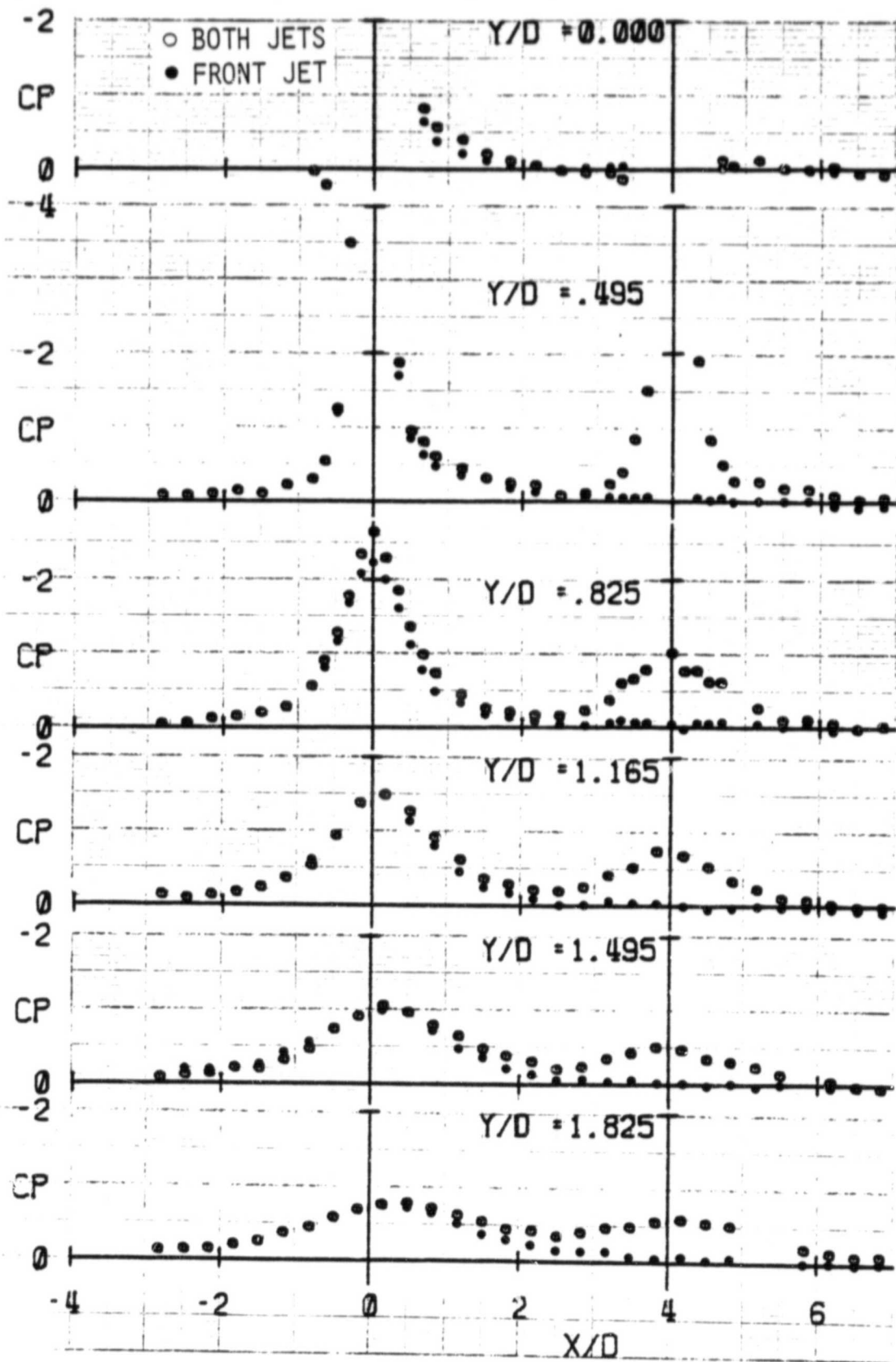


Fig. 29 - Surface Pressure Distribution
(ΔC_p): Flat Plate Model,
90 deg., $R = 6$, $S/D = 4$.

ORIGINAL PAGE 13
OF POOR QUALITY

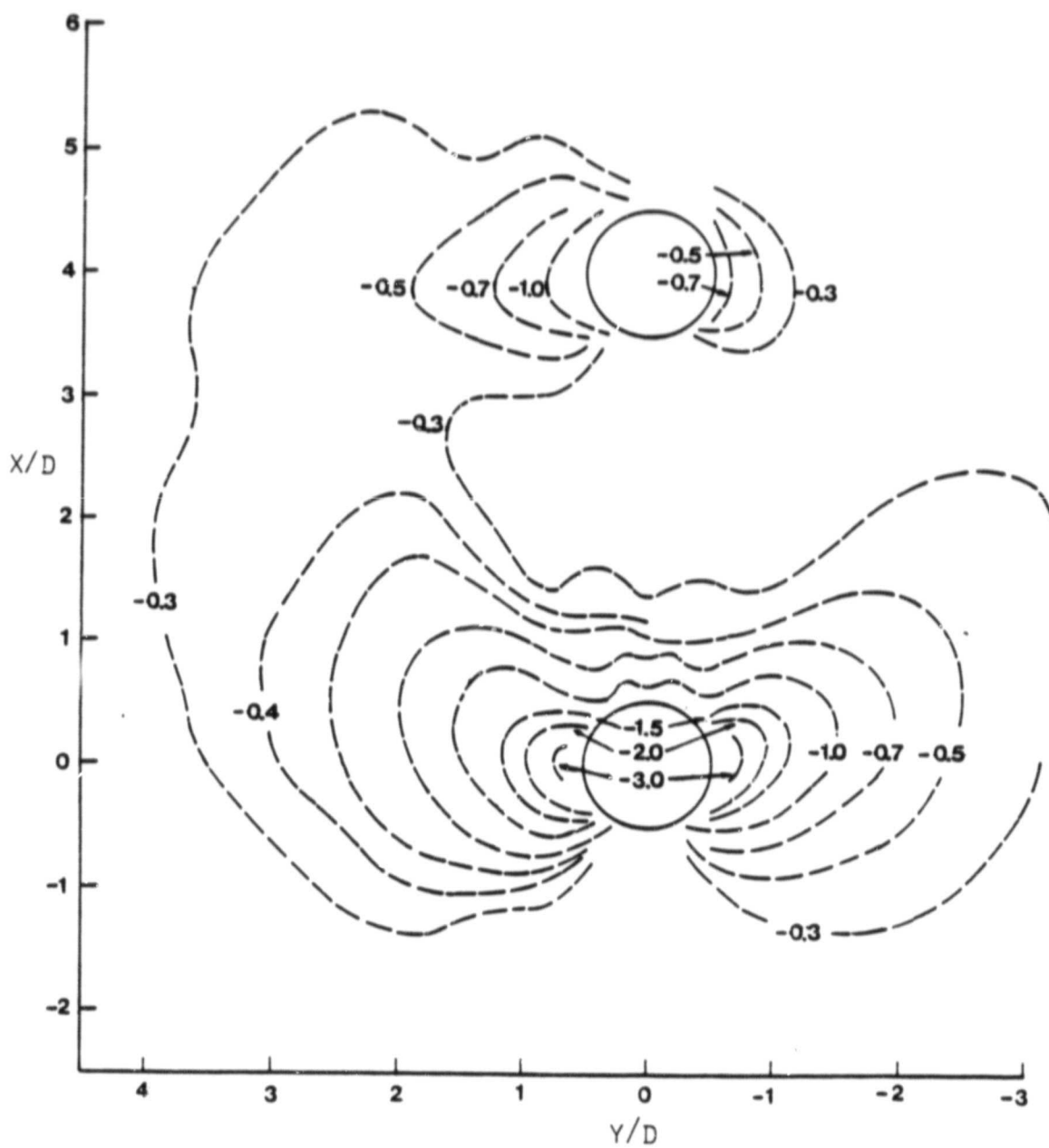


Fig. 30 - Isobar Map of ΔC_p : Flat
Plate with Both Jets,
90 deg., $R = 6$, $S/D = 4$.

ORIGINAL PAGE IS
OF POOR QUALITY

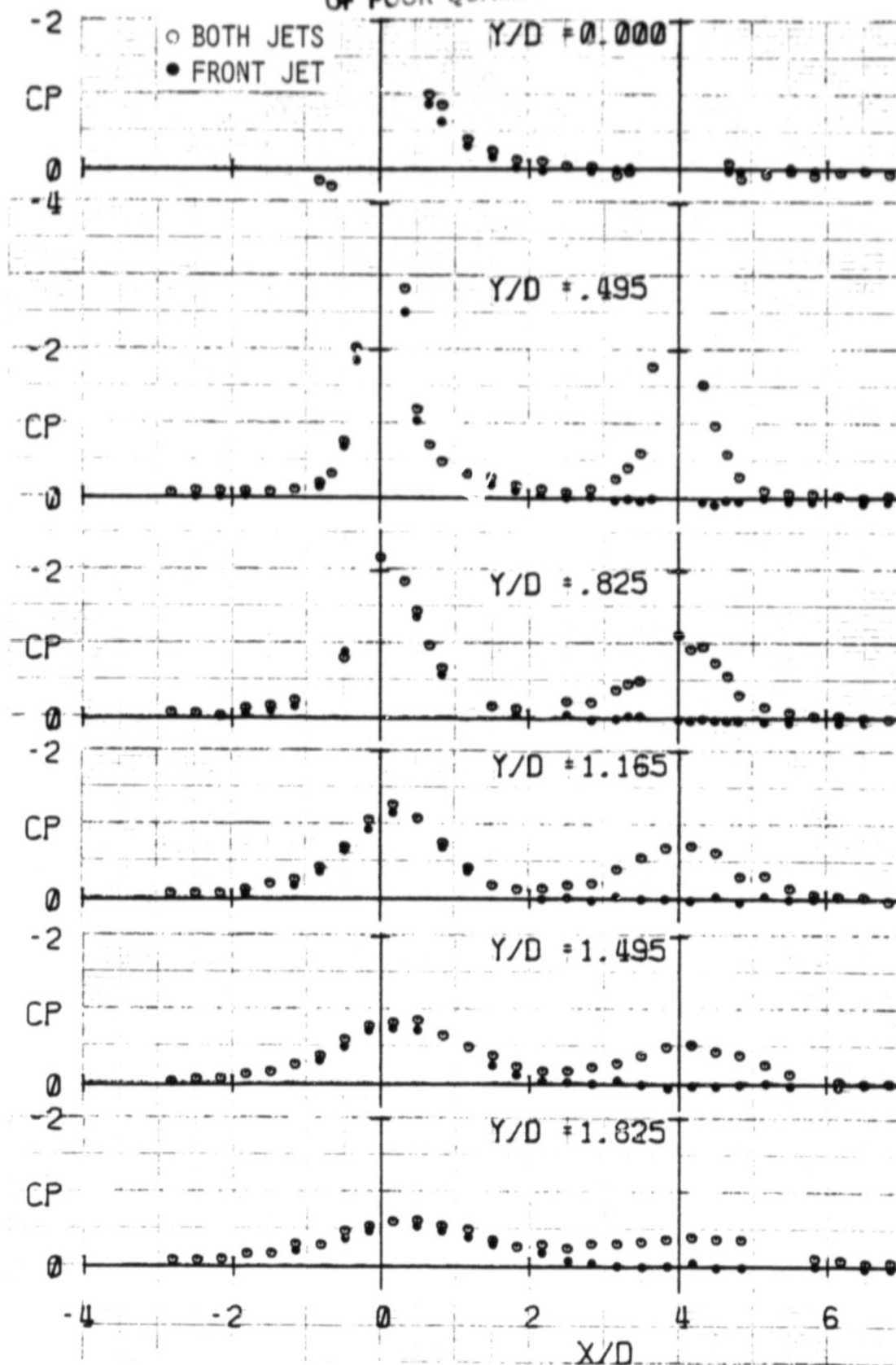


Fig. 31 - Surface Pressure Distribution
(ΔC_p): Flat Plate Model,
75 deg., $R = 6$, $S/D = 4$.

ORIGINAL PAGE IS
OF POOR QUALITY

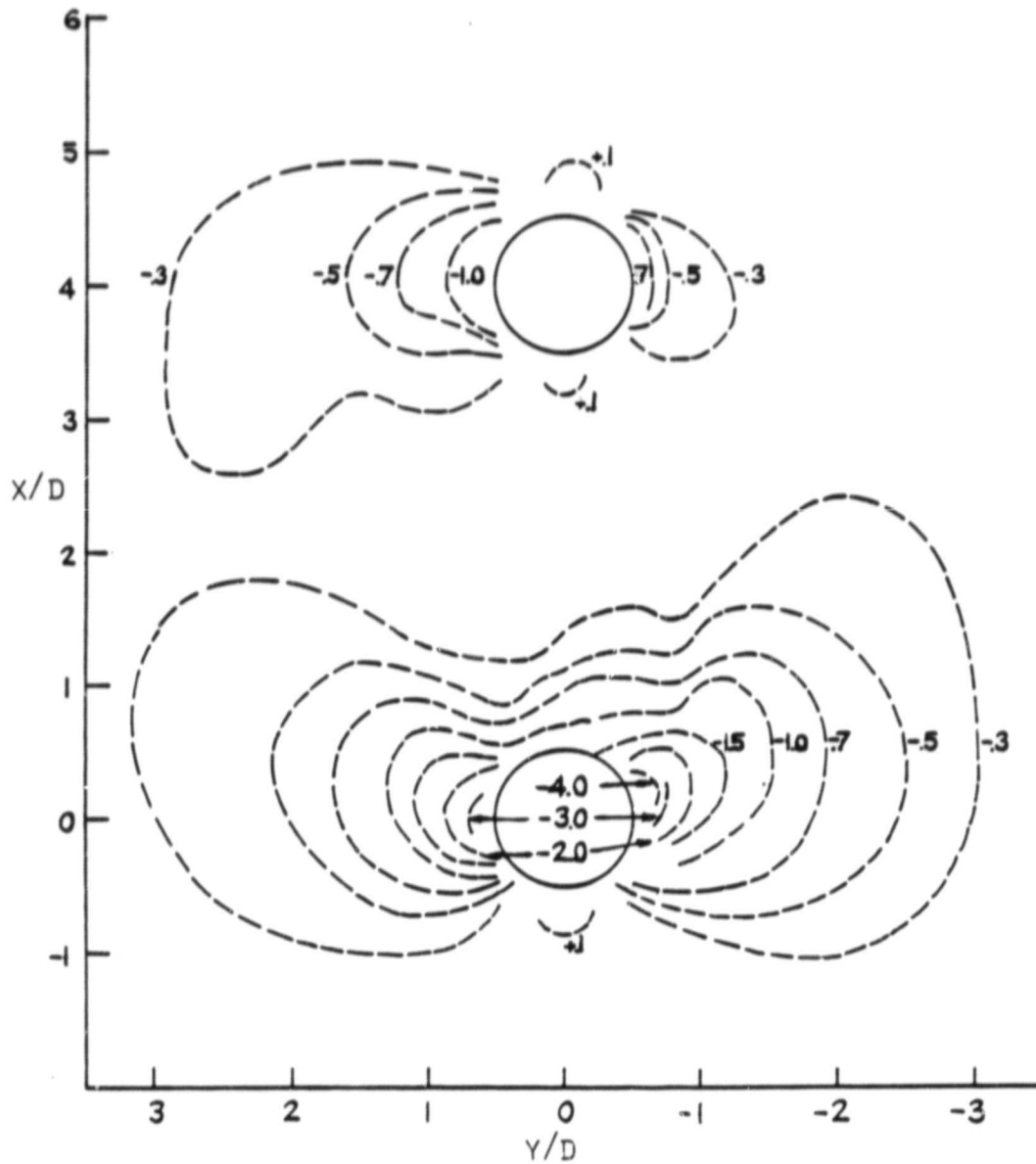


Fig. 32 - Isobar Map of ΔC_p : Flat
Plate with Both Jets,
75 deg., $R = 6$, $S/D = 4$.

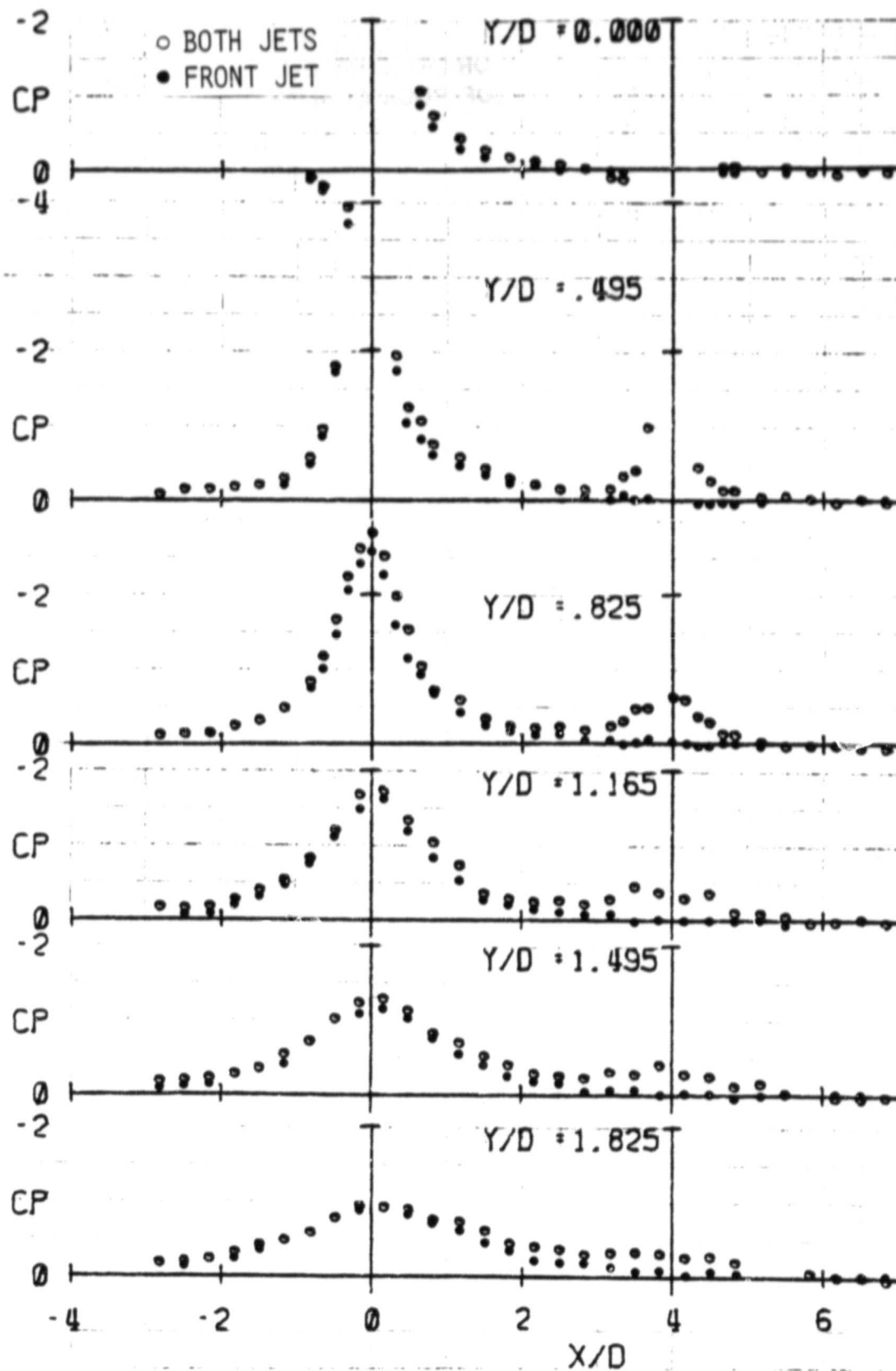


Fig. 33 - Surface Pressure Distribution
(ΔC_p): Flat Plate Model,
105 deg., $R = 6$, $S/D = 4$.

ORIGINAL PAGE IS
OF POOR QUALITY

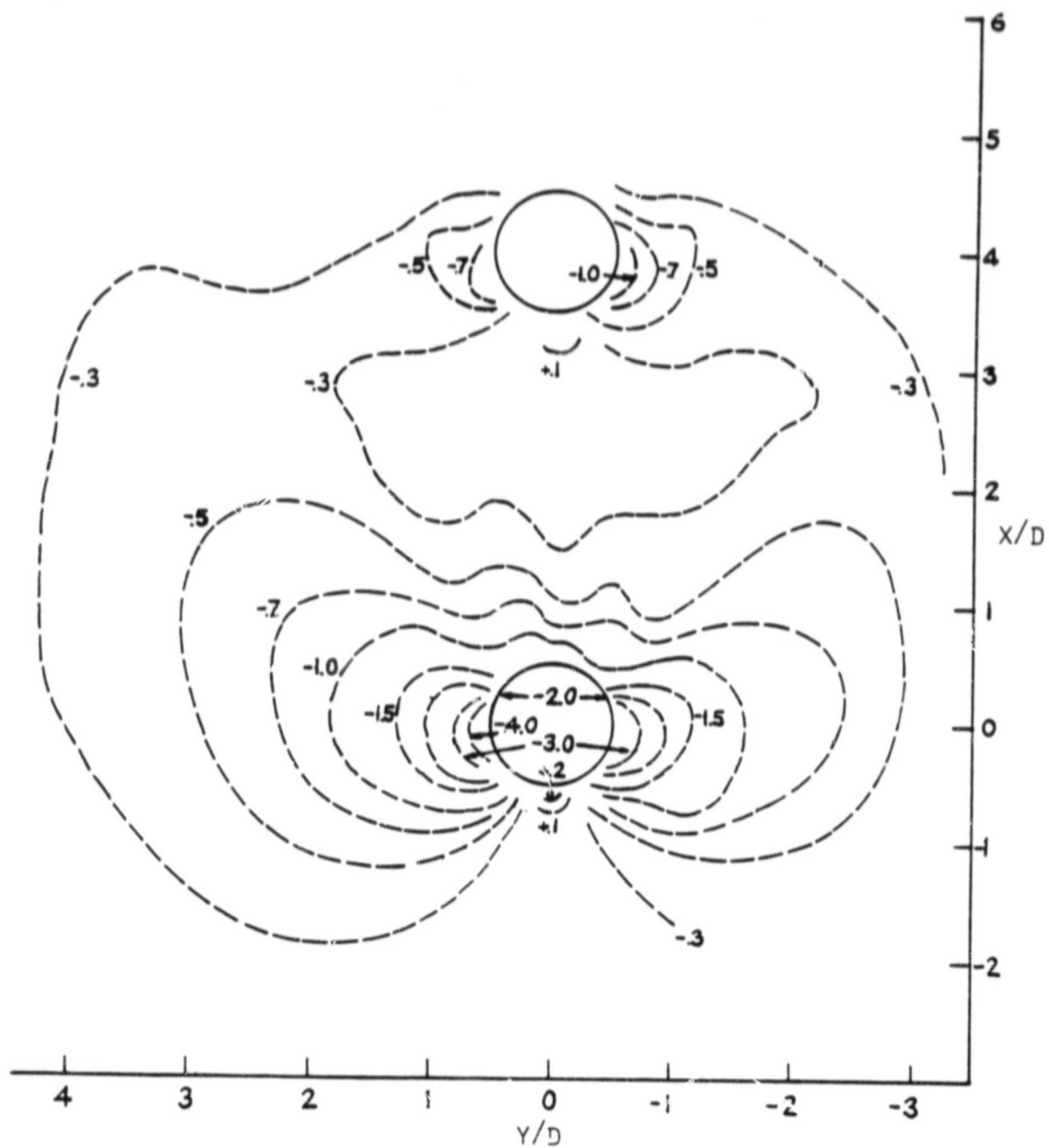


Fig. 34 - Isobar Map of C_p : Flat
Plate with Both Jets,
105 deg., $R = 6$, $S/D = 4$.

ORIGINAL PAGE IS
OF POOR QUALITY

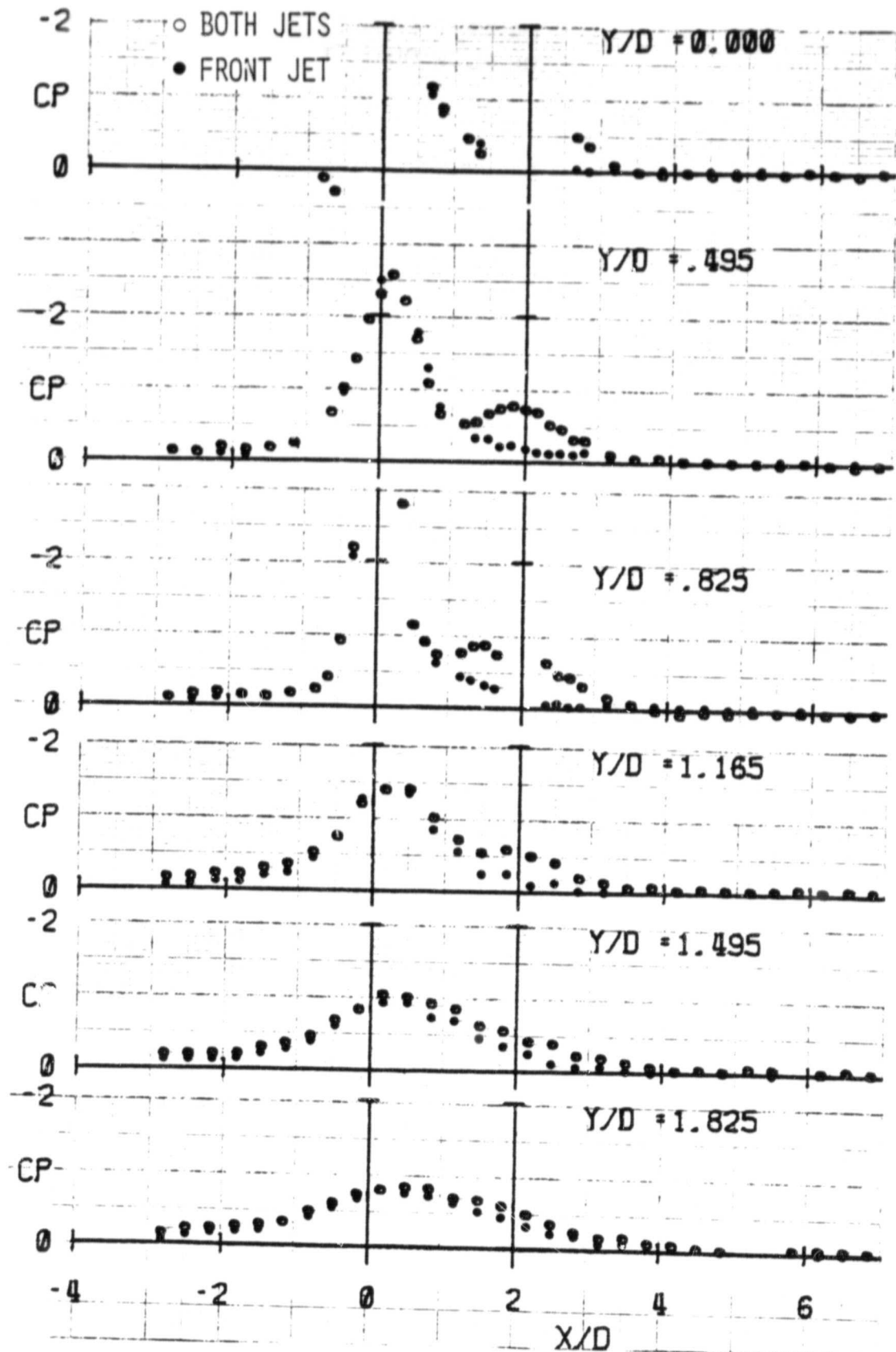


Fig. 35 - Surface Pressure Distribution
(ΔC_p): Flat Plate Model,
75 deg., $R = 6$, $S/D = 2$.

ORIGINAL PAGE IS
OF POOR QUALITY

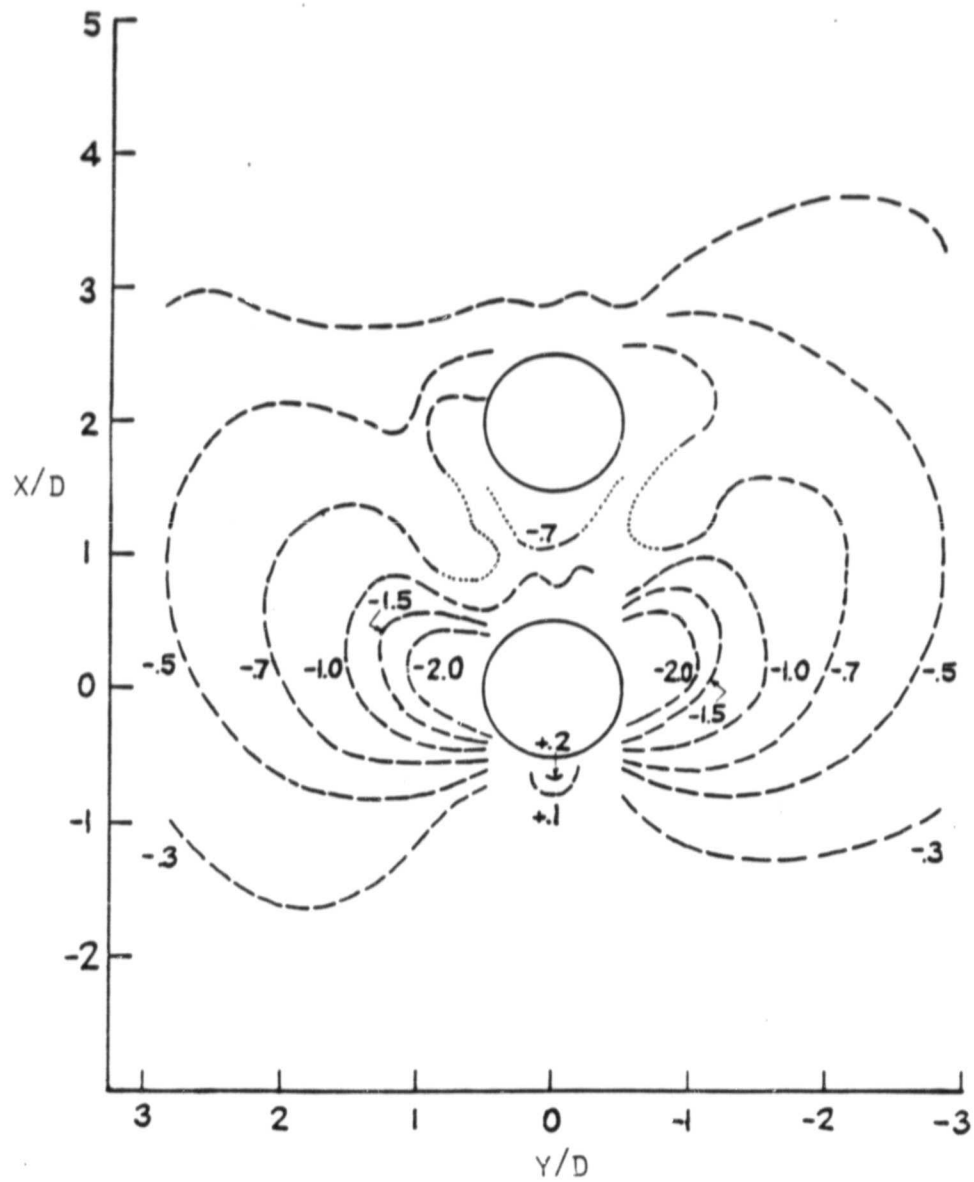


Fig. 36 - Isobar Map of ΔC_p : Flat
Plate with Both Jets,
75 deg., $R = 6$, $S/D = 2$.

ORIGINAL PAGE IS
OF POOR QUALITY

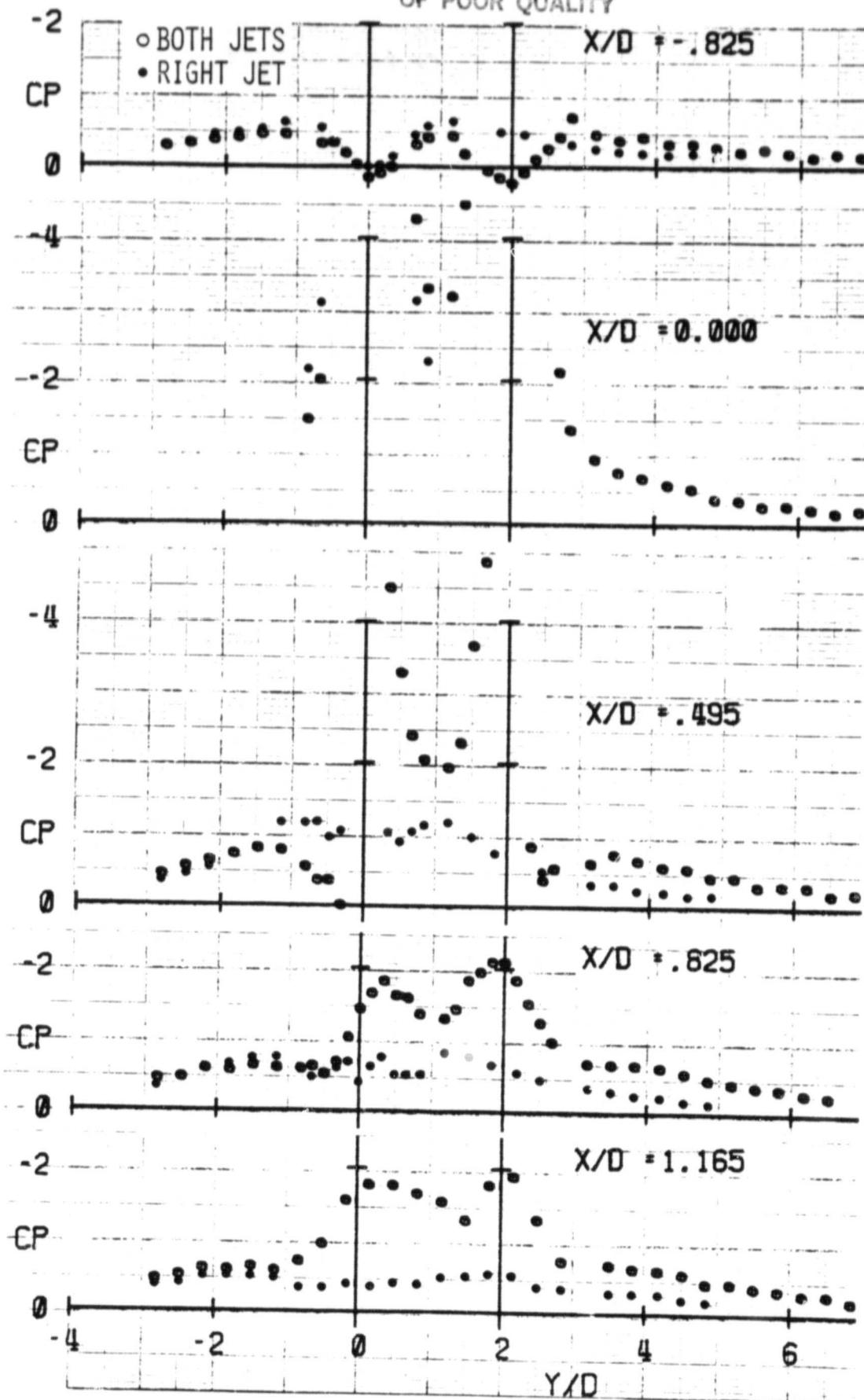


Fig. 37 - Transverse Surface Pressure Distribution (ΔC_p): Flat Plate Model, 90° , $R = 6$, $S/D = 2$, Side-by-Side.

ORIGINAL PAGE IS
OF POOR QUALITY

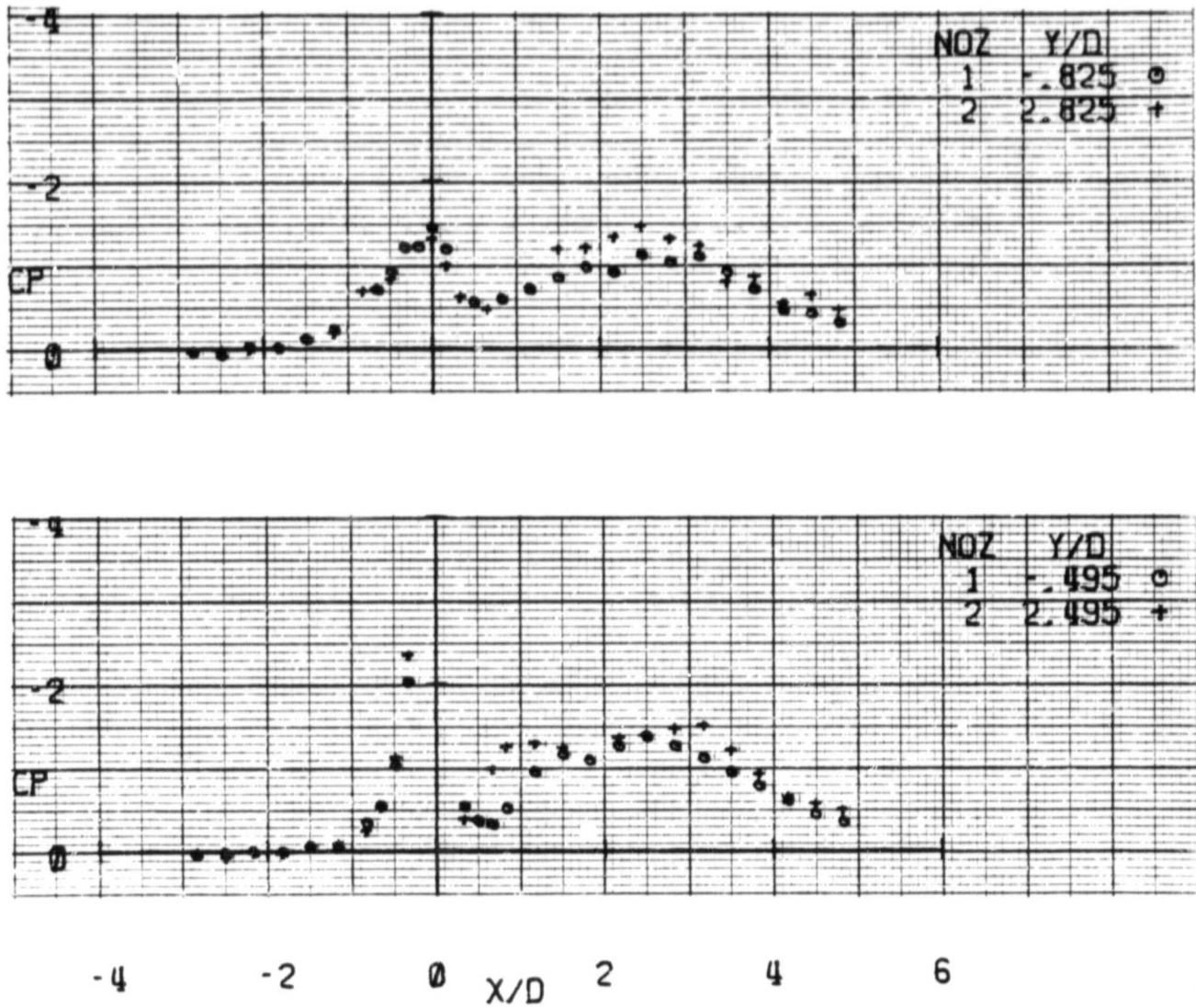


Fig. 38 - Axial Surface Pressure
Distributions (ΔC_p): Flat
Plate Model, 90 deg., $R = 6$,
 $S/D = 2$, Side-by-Side.

70

ORIGINAL PAGE IS
OF POOR QUALITY

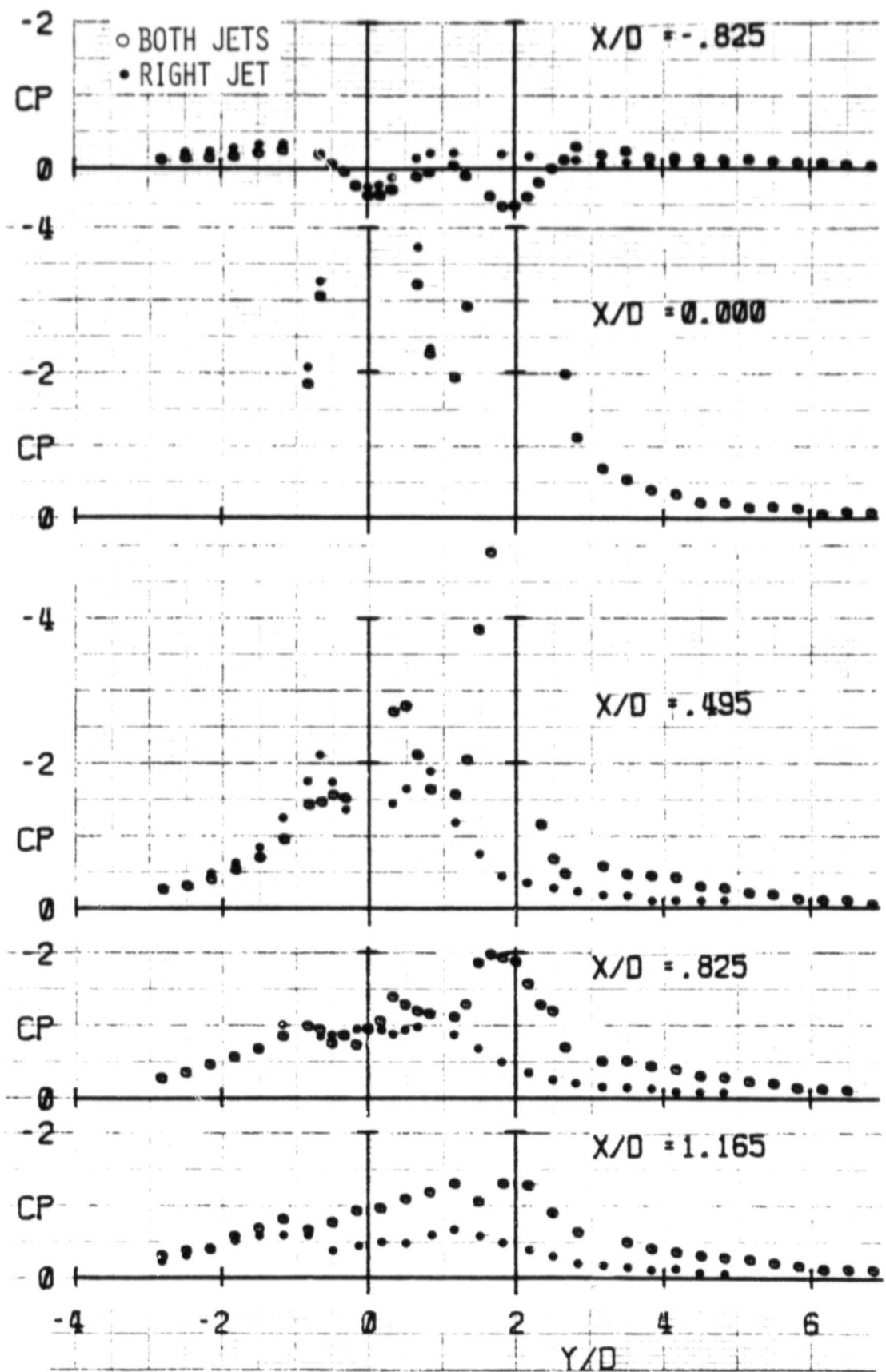


Fig. 40 - Transverse Surface Pressure Distribution (ΔC_p): Flat Plate Model, 90 deg., $R = 4$, $S/D = 2$, Side-by-Side.

ORIGINAL PAGE IS
OF POOR QUALITY

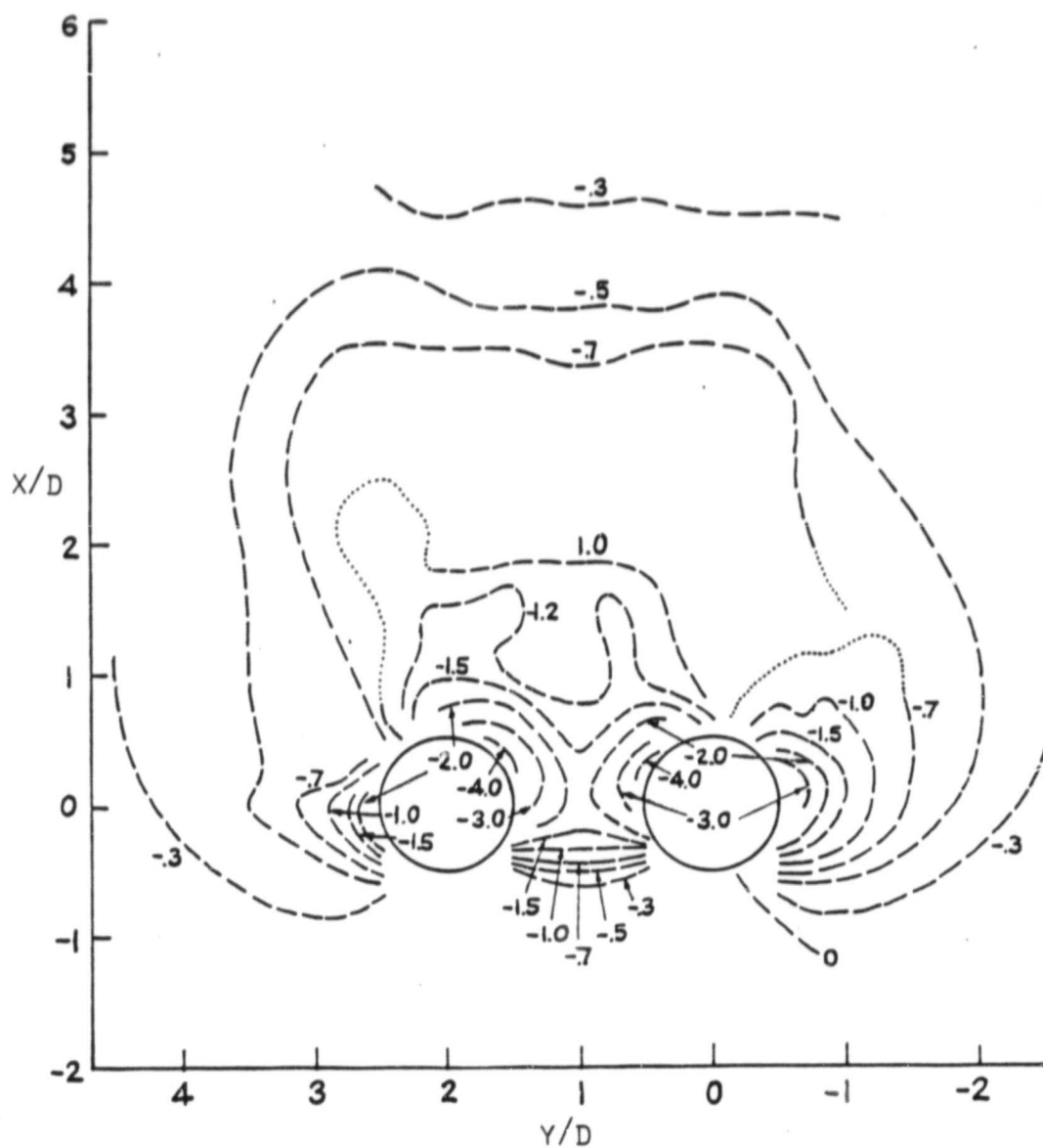


Fig. 41 - Isobar Map of ΔC_p : Flat
Plate with Both Jets, 90 deg.,
 $R = 4$, $S/D = 2$, Side-by-Side.

ORIGINAL PAGE 13
OF POOR QUALITY

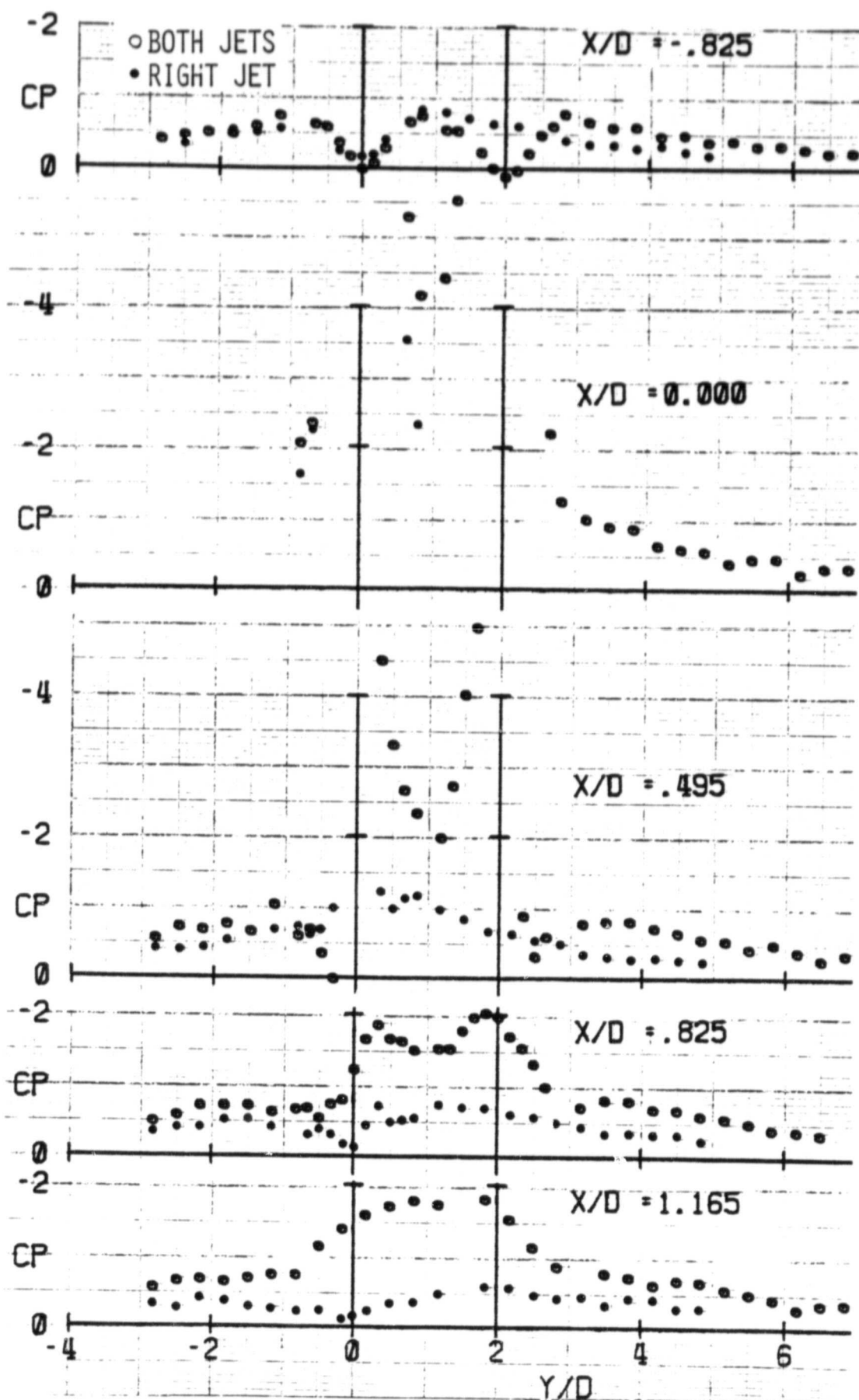


Fig. 42 - Transverse Surface Pressure Distribution (ΔC_p): Flat Plate Model, 90 deg., $R = 8$, $S/D = 2$, Side-by-Side.

ORIGINAL PAGE IS
OF POOR QUALITY

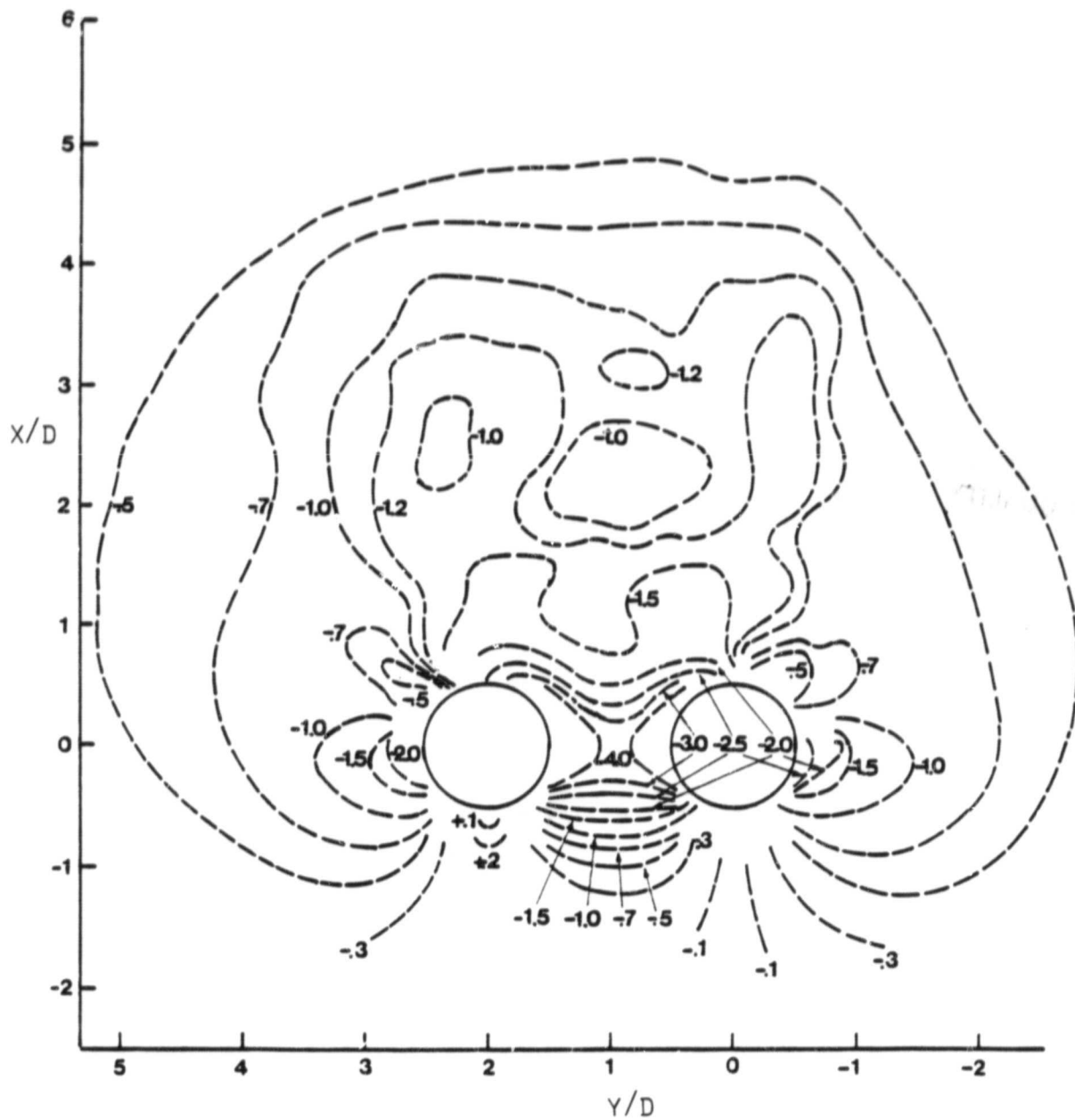
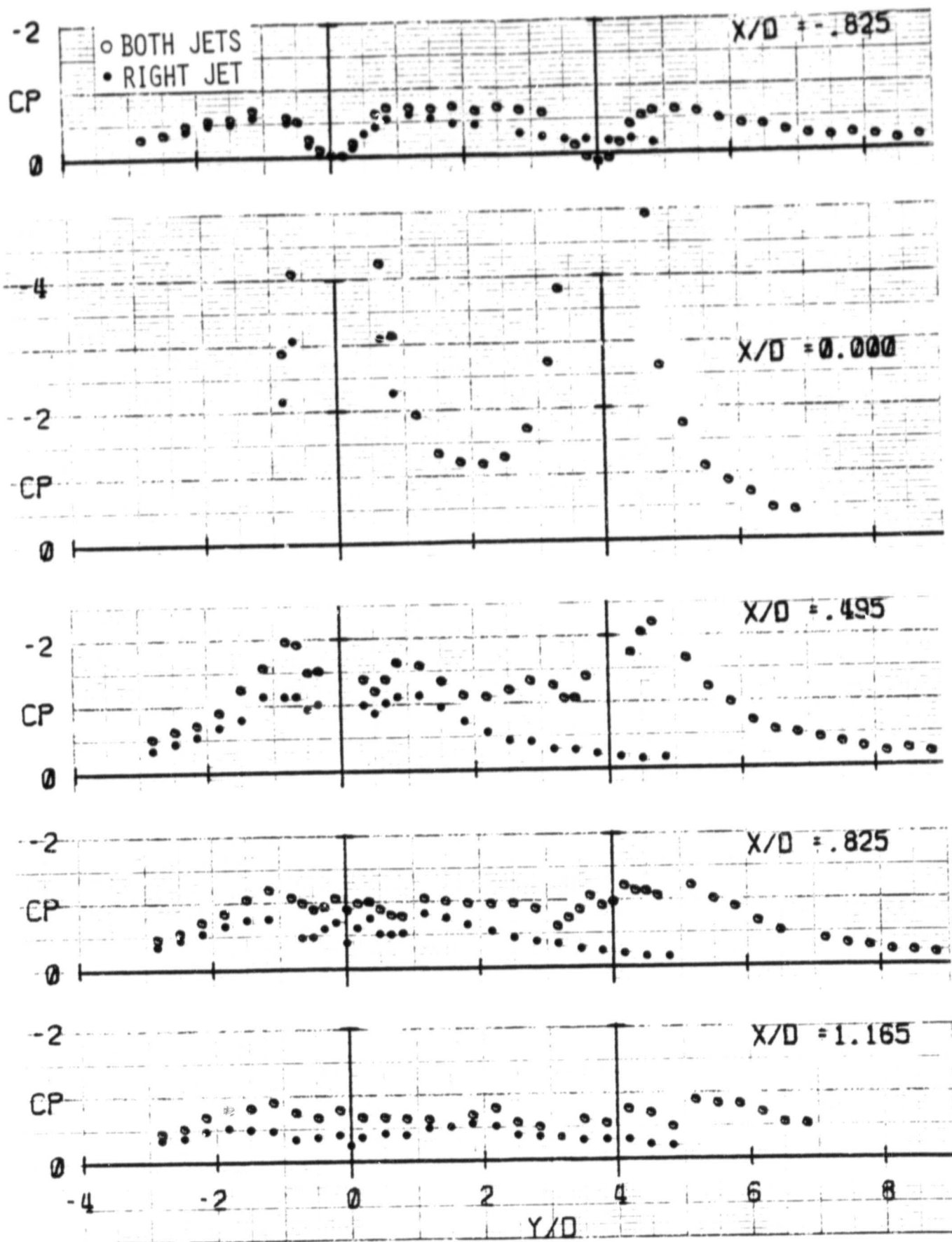


Fig. 43 - Isobar Map of ΔC_p : Flat
Plate with Both Jets, 90 deg.,
 $R = 8$, $S/D = 2$, Side-by-Side.



ORIGINAL PAGE 13
OF POOR QUALITY

Fig. 44 - Transverse Surface Pressure Distribution (ΔC_p): Flat Plate Model, 90 deg., $R = 6$, $S/D = 4$, Side-by-Side.

ORIGINAL PAGE IS
OF POOR QUALITY

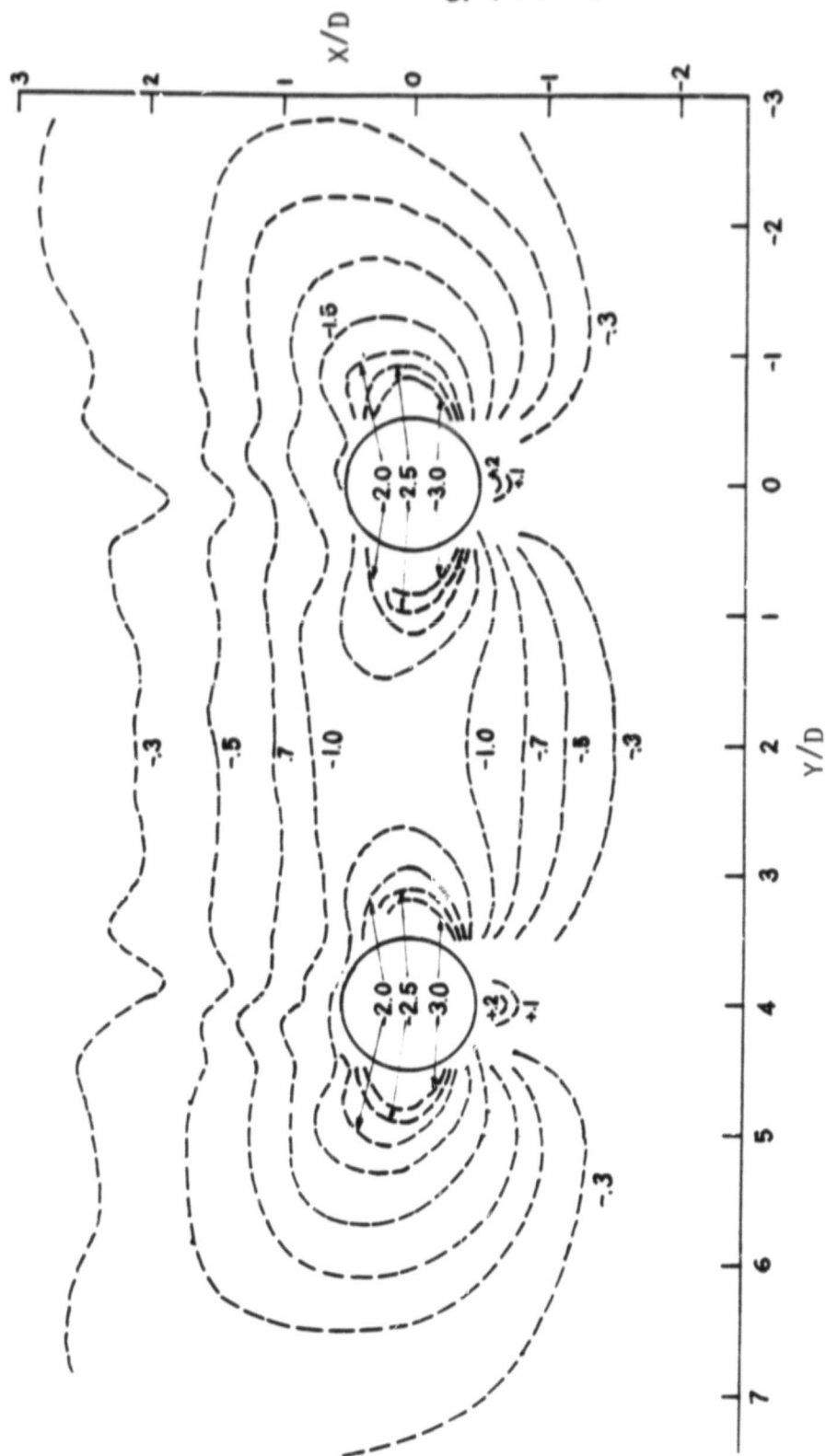


Fig. 45 - Isobar Map of ΔC_p : Flat
Plate with Both Jets, 90 deg.,
 $R = 6$, $S/D = 4$, Side-by-Side.